

## Quantum size effect on ultra-thin metallic films

This article has been downloaded from IOPscience. Please scroll down to see the full text article.

2010 J. Phys. D: Appl. Phys. 43 013001

(<http://iopscience.iop.org/0022-3727/43/1/013001>)

View [the table of contents for this issue](#), or go to the [journal homepage](#) for more

Download details:

IP Address: 140.109.103.227

The article was downloaded on 25/05/2011 at 05:25

Please note that [terms and conditions apply](#).

## TOPICAL REVIEW

# Quantum size effect on ultra-thin metallic films

W B Su, C S Chang and Tien T Tsong

Institute of Physics, Academia Sinica, Taipei 115, Taiwan, Republic of China

Received 16 March 2009, in final form 6 October 2009

Published 14 December 2009

Online at [stacks.iop.org/JPhysD/43/013001](http://stacks.iop.org/JPhysD/43/013001)**Abstract**

When the thickness of a metallic film is in the nanometre range, electrons in the film as well as those transmitting through the film can both manifest the quantum size effect (QSE). For the former, electrons are confined in the quantum well of a metal film to form quantum-well states. For the latter, electrons scattered by the quantum well in the film can bring about the phenomenon of transmission resonance. Scanning tunnelling microscopy (STM) combined with spectroscopy is a powerful tool to explore these two kinds of QSE. In this paper, we review our recent studies on the QSE of thin Pb and Ag films by using STM. We demonstrate that the formation of the quantum-well states in the Pb film can significantly affect the morphology, thickness, growth process and electronic structures of Pb films. On the other hand, the transmission resonance can be observed on the Ag film with  $Z$ - $V$  spectroscopy in STM. The energy level of the transmission resonance varies with the film thickness and can be shifted by the electric field. Moreover, in the studies of transmission resonance, it is unavoidable to observe the standing-wave states, i.e. Gundlach oscillations, which are the QSE in the tunnelling gap. We have also discovered that the Gundlach oscillation can be exploited to measure the work function of thin metal films with very high precision.

(Some figures in this article are in colour only in the electronic version)

**1. Introduction**

Metallic films with atomic-scale flatness have attracted intense studies for years due to both scientific interest and possible applications in the integrated circuit industry. In particular, when the thickness of the metallic film is comparable to the de Broglie wavelength of electron, the electronic structure of the metallic film will be significantly modified because of the manifestation of the quantum behaviour (wave nature) of electrons. This, named the quantum size effect (QSE), may render the physical properties of the metallic films evidently different from those of the bulk and have potential applications for nanotechnology.

The QSE of the metallic films is basically related to the issue of one-dimensional square well in quantum mechanics. There are two kinds of situations, depending on which the electron is either confined in the well or scattered by the well. Owing to the wave nature of the electron, for the former case, the energy level of the electron in the well is not the continuum

but is the discrete quantum-well (QW) states. For the latter case, the transmission probability for the free electron passing through the well may reveal an oscillatory behaviour with increasing electron kinetic energy. The highest transmission probability is called the transmission resonance. These two kinds of quantum phenomena can be explored experimentally on some metallic films because their inert potential can be approximated by a square well. Technically, one can use the photoemission spectroscopy to study the former case [1–5] and use the low energy electron transmission spectroscopy [6] to study the latter case [7, 8]. Using scanning tunnelling microscopy (STM) combined with spectroscopy [9], however, both kinds of QSE can be investigated. This is due to the fact that STM is a technique probing the density of states of the sample, and therefore, the QW states of the thin films in both empty and filled states can be detected. On the other hand, when one adjusts the bias voltage in STM to tune the Fermi level of the tip to be beyond the vacuum level of the film, electrons leaving from the tip can be of the kinetic energy,

and therefore the QSE of electron scattered by the quantum well, i.e. the transmission resonance can be explored with the  $Z$ - $V$  spectroscopy. The electron tunnelling from the tip is at the field-emission regime when the Fermi level of the tip is above the vacuum level of the sample. At this situation, the potential well in the tip-sample gap is the superposition of the image potential and applied potential. Electrons in the well can manifest another kind of the QSE similar to the QW states, i.e. the energy levels are quantized and the standing wave states are formed. When the applied bias voltage matches the energy level of the standing wave state, the field-emission current would rapidly increase to reveal the resonance. Therefore, the measured current varies in oscillation with the bias voltage, which was first predicted by Gundlach [10]. Thus, this field-emission resonance through the standing wave state is also named Gundlach oscillation. While the QW states and the transmission resonance can be observed using other techniques, the Gundlach oscillation can only be studied by  $Z$ - $V$  spectroscopy in STM. In addition, since the standing wave state exists in the tunneling gap, one can observe the Gundlach oscillation on both the thin film [11] and the crystal surfaces [12–14].

An intuitive starting point for an investigation of the QW states and the transmission resonance is to prepare a flat metallic film with a well-defined thickness on the semiconductor. However, because of the lattice mismatch, the stress existing at the metal/semiconductor interface may drive the morphology of the metal film to be three-dimensional (3D) islands instead of a flat film. Fortunately, recent discoveries have demonstrated that 3D growth behaviour can be changed into the formation of the flat films by introducing the way of the low-temperature deposition followed by annealing at room temperature. By this procedure, atomically flat Ag films with the preferred thickness of seven and two atomic layers have been created on the GaAs (110) and Si(111) surfaces, respectively [15, 16]. However, the procedure of annealing at room temperature is not always necessary. Later studies by using the spot analysis low energy electron diffraction (SPA-LEED) demonstrate that actually flat Pb islands with the preferred thickness of seven atomic layers can be directly grown on the Si(111)7 × 7 surface at a low temperature of 185 K [17]. Moreover, flat Ag films can be grown on the Si(111)7 × 7 surface at room temperature [18]. Therefore, these previous studies have shown us the ways of preparing the flat metallic films on semiconductors for studying the QSE.

In this paper, we review our recent STM and spectroscopic studies on these three kinds of QSE. The QW state and the transmission resonance have observed on Pb and Ag films, respectively. The Gundlach oscillation have been studied on Ag films and crystal surfaces of Au(111) and Ag(100). The rest of this review is arranged as follows. In section 2, we introduce the influence of the QSE on the growth behaviour of Pb films. That is, we need to prepare flat Pb films for studying the QW states but we have observed that the existence of the QW states can return to affect the growth behaviour of Pb films. We thus have found unusual growth characteristics different from the conventional growth mode, such as the preferred thickness [19, 20], the multi-layer islands with the

two-dimensional (2D) growth behaviour [21] and the 3D-to-2D growth transition [22]. In section 3, we introduce the influence of physical properties of the real system on the QSE. Since the QSE is observed in real systems, its behaviour will be affected by the properties of the system. We have found that the strength of the QW states is modulated by the periodic distortion in the film [23], the energy level of the transmission resonance [24] is shifted by the electric field [25] and the peak intensity of the Gundlach oscillation is modulated by the interface structure and the surface reconstruction [26]. In section 4, we introduce that the Gundlach oscillation can be a precise way of measuring the work function of the metallic film [27].

## 2. Influence of the QSE on the growth behaviour of Pb films: quantum-well states

Pb is known to be chemically inactive and it does not intermix with Si [28]. Therefore, the Pb/Si interface is sharp, which facilitates the studies of the growth mechanism and the electronic properties. For Pb deposition at room temperature on the Si(111)7 × 7 surface at low coverage, Ganz *et al* found that Pb atoms occupy sites above the rest atoms and between the Si adatoms with a preference for the faulted half of the unit cell [29]. Gómez-Rodríguez *et al* demonstrated that the Pb atom pairs are mobile at room temperature within the half 7 × 7 unit cell, and an activation energy of 0.40 eV was measured for this thermally activated process [30]. When the annealing is performed after the deposition of Pb on the Si(111)7 × 7 surface, the Si(111)7 × 7 surface can be converted into a 1 × 1 bulk-terminated structure. And the different phases of Pb atoms on the Si(111) surfaces at room temperature can be formed with varying degrees of coverage up to 2 monolayer (ML) [28, 31–35]. These studies show that a mosaic  $\sqrt{3}$  phase can be observed at 1/6 ML. At 1/3 ML, the  $\sqrt{3} \times \sqrt{3}$  phase is formed. Between 1/3 and 1 ML a 1 × 1 Pb overlayer coexists with the 1/3 ML  $\sqrt{3}$  phase, while above 1 ML there appears incommensurate phase. In addition, Heslinga *et al* reported that the Schottky-barrier height of the Pb overlayer for the Si(111)7 × 7-Pb structure is different from that for the Si(111)  $\sqrt{3} \times \sqrt{3}$ -Pb structure, and the former is 0.7 eV and the latter is 0.93 eV [36]. At higher coverage, Pb is known to grow on Si(111) with the Stranski–Krastanov mode at room temperature, i.e. to grow in 3D islands following the completion of a wetting layer. By increasing the coverage up to hundreds of ML, the islands start to connect to each other and finally a continuous film is formed [31]. However, the growth behaviour of Pb films at low temperature is very different from that at room temperature. Budde *et al* have observed that flat Pb islands with a thickness of seven atomic layers can be grown on the Si(111)7 × 7 surface at 185 K [17]. A specific characteristic of this growth phenomenon, not observed in the conventional growth, is that islands have the preferred thickness to grow. This peculiar growth feature can be explained by a model named ‘electronic growth’ proposed by Zhang *et al* [37]. The essence of this model is based on the QSE in the metal film and the inclusion of charge spilling occurring at the metal/semiconductor interface. According to this model, a metal layer can be stabilized by the quantum

confinement, but it can also be destabilized by a charge spilling from the metal to the semiconductor. The competition between these two effects results in the appearance of the preferred thickness. Therefore, one needs to prepare flat metal films for studying the QW states but aforementioned experimental observations and the electronic growth model show that the QSE can manifest itself in the metal film to affect the growth behaviour of the films.

The manifestation of the QW states in the electronic structure can result in many properties of the film being different from that of the bulk. For instance, Schulte [38] earlier calculated the film thickness dependence of the electron densities, the potentials and the work functions for freestanding metal films and found oscillation in all these quantities. This prediction was experimentally studied later by different techniques. For example, Jaklevic *et al* discovered the periodic structure in the electron tunnelling spectra of Pb, Mg, Au and Ag films, revealing a direct observation of thickness-dependent electronic states in thin metal films [39]. Marliere measured the work function of the indium film and found the work function varying with the film thickness [40]. Jałochowski *et al* found the oscillation of the electrical resistivity of thin epitaxial Pb films on the Si(1 1 1) surfaces. They attributed the oscillation to the quantization of the Fermi momentum of the film electrons [41]. Because of the existence of the QW states, the electronic structures of metallic films may vary with thickness, which have been observed using photoemission spectroscopy [42, 43]. Moreover, the QW state always accompanies with the formation of the standing wave in metallic films. The studies of He scattering and STM [19, 44, 45] have demonstrated that the film may relax in order to make its thickness match the multiple half wavelength, causing that the interlayer spacing varies with the thickness in oscillation. Recent studies have shown that the QSE can affect other physical properties of metallic films. For instance, Luh *et al* used photoemission spectroscopy to study the thermal stability of the Ag films on the Fe(1 0 0) surface [46]. They discovered that films with some specific thicknesses are thermally stable in comparison with other thicknesses. Guo *et al* [47] and Eom *et al* [48] have observed that the superconducting transition temperature of the Pb film on the Si(1 1 1) surface changes with film thickness. They attributed the variation of the transition temperature to the density of states oscillation at the Fermi level. Chan *et al* [49] and Ma *et al* [50] observed the adatom diffusion barrier on Pb films, and they have found that the diffusion barrier can vary with film thickness in oscillation. Jeffrey *et al* used surface x-ray scattering and STM to observe the coarsening behaviour of Pb nanocrystals [51]. They have found that the QSE leads to the breakdown of the classical Gibbs–Thomson analysis. Fu *et al* used STM and spectroscopy to observe the Kondo resonance of individual manganese phthalocyanine (MnPc) molecules adsorbed on the top of Pb islands [52]. They have discovered the oscillating Kondo temperatures as a function of film thickness. Lin *et al* used STM to observe the growth of Ag on Pb quantum islands [53]. They have observed that electronic Moiré patterns found on the island can serve as a template to grow self-organized Ag clusters (nanopucks). Zhang *et al* performed the varied temperature photoemission

study to investigate the thermal property of atomically flat Pb films grown on Si(1 1 1) [54]. They have found that the thermal expansion coefficient of the Pb film varies with the thickness due to the QSE.

The observation of SPA–LEED [17] motivates us to use STM to examine the growth of Pb islands in the real space. Our results show that flat-top Pb islands of thickness confined in the range 4–9 atomic layers can be formed and the 7-layer island is the most abundant one. In addition,  $I$ – $V$  spectroscopic measurements on individual islands reveal the QW states, manifesting that the QSE indeed exists in Pb islands [19]. Furthermore, we also explore the essential factors influencing the growth of islands such as the coverage, temperature and interface [20, 21]. From the observation of growth process of an individual island, we find out that there exists a transition from 3D to 2D growth [22]. This growth transition is induced by the QSE as well.

The experiment was carried out in a UHV chamber (base pressure less than  $1 \times 10^{-10}$  mbar) equipped with a cold-finger type variable temperature STM and a well-collimated e-beam heating evaporator of high purity Pb. Samples were cut from boron doped Si(1 1 1) wafers with the resistivity of 0.1–1  $\Omega$  cm and a miscut angle of less than  $0.1^\circ$ . The reconstructed  $7 \times 7$  surface was obtained by annealing samples to 1200  $^\circ$ C and followed slow cooling to room temperature. Lead atoms were evaporated onto the predetermined sample at low temperatures with a rate of 0.16 ML  $\text{min}^{-1}$ . The pressure was kept below  $2 \times 10^{-10}$  mbar during the deposition. To prepare the incommensurate  $\sqrt{3}$  surface, 2 ML of Pb was first deposited onto the  $7 \times 7$  surface at room temperature and followed by annealing at 480  $^\circ$ C for a few seconds.  $I$ – $V$  spectra were obtained by interrupting the STM feedback loop every five pixel points in the scan. During spectra acquisitions, in order to reduce the thermal broadening, the sample was cooled to 50 K.

### 2.1. Growth characteristics

Figure 1(a) shows a typical STM topography image of a Pb film grown at 208 K with a coverage of 3.2 ML. Before the formation of islands, about 2 ML of Pb are consumed in wetting the Si(1 1 1)  $7 \times 7$  substrate. The rest of Pb grows into islands with steep edge above the wetting layer. The surface of the islands is very flat and its orientation is along the [1 1 1] direction [55]. The contrast of the image also implies that the thickness of the island is not the same. In order to understand the distribution of the island thickness and the variation of the distribution with coverage, we sampled hundreds of islands to analyse their thickness at each coverage. Figure 1(b) shows the ratio distribution as a function of island thickness at three coverages. It is interesting to note that the thickness of islands is confined within the range 4–9 atomic layers, and islands with 7-layer thickness are the most abundant, consistent with the SPA–LEED observation [17]. We analyse the average thickness of islands and it only increases  $\sim 7\%$  even though the coverage (above wetting layer) increases by a factor of 3. This indicates that the growth of islands is mostly along the lateral direction. Figure 1(c) demonstrates that the average area of the

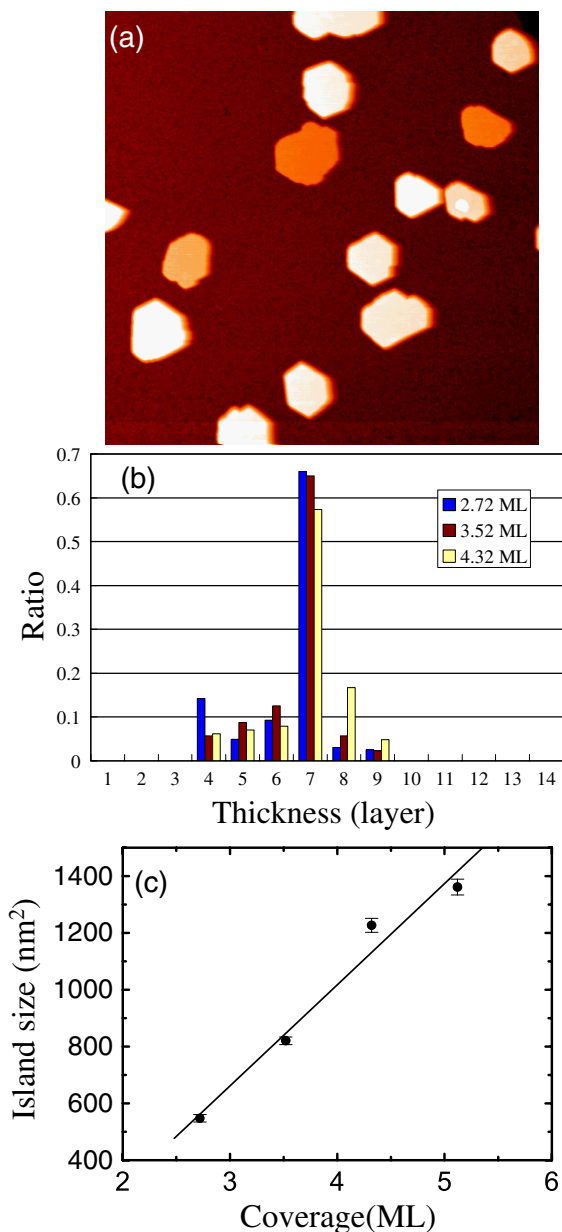


**Figure 1.** (a) Pb islands created by depositing 3.2 ML of Pb at 208 K on the Si(111)7 × 7 surface (image size: 3000 × 3000 Å<sup>2</sup>). (b) The appearance ratios as a function of island thickness at three different coverages. (c) The average size of islands linearly increases with coverage at the saturated regime, showing a quasi-two-dimensional growth behaviour.

islands increases with coverage linearly, further illustrating the 2D growth behaviour of these islands. In addition, it is worth to emphasize that the appearance of the preferred thickness should accompany with the 2D growth of Pb islands because increasing coverage is to increase the area once the thickness is restricted. This implies that 2D growth is driven by the QSE as well.

### 2.2. Formation of multi-layer Pb islands: from nucleation to growth

An unusual characteristic of Pb islands is their lack of thickness below four layers, implying that the growth should not be

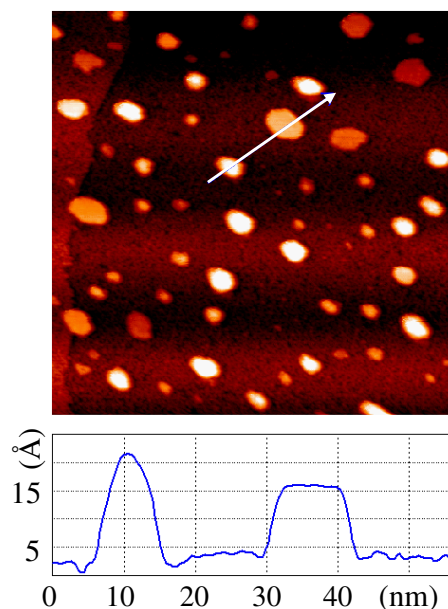


**Figure 2.** STM image with 2.32 ML Pb on the Si(111)7 × 7 surface at 170 K, showing 3D clusters and 2D islands are formed concurrently on the wetting layer. The line profile across a cluster, indicated by an arrow in STM image, shows a 3D morphology (image size: 300 nm × 300 nm).

the layer-by-layer mode even though their top surface is flat. This motivates us to explore the process of how Pb islands are created from initial nucleation to growth. In order to investigate this issue, we observe the growth stage right after the completion of the wetting layer at a lower temperature of 170 K. Figure 2 shows the STM image of 0.32 ML Pb above wetting layer. It can be seen that clusters and flat islands are formed concurrently on the wetting layer. The line profile across a cluster and an island in figure 2, indicated by an arrow, shows the 3D morphology of the cluster and flat-top surface of the island. This observation implies that the clusters may be the seeds for growing islands. In order to confirm this point, we *in situ* observe the growth process of an individual island with STM. Figures 3(a)–(c) show the growth of two 3D clusters as marked by numbers in figure 3(a) with increasing coverage. Line profiles at the right side of corresponding STM images represent the morphology evolution of clusters 1 and 2 along the arrows. After twice deposition of 0.02 ML, cluster 1 with a height of 9.1 Å in figure 3(a) transformed into a flat-top island with an 11.3 Å thickness, then grew to a larger island of the same thickness, as shown in figures 3(b) and (c), respectively. On the other hand, cluster 2 of 15.9 Å height grew into a higher cluster of 20.5 Å height, then transformed into an island with a 20.4 Å thickness. Therefore, islands are indeed grown from clusters. Moreover, figure 3 reveals that an island thickness can be directly correlated with a cluster height before transition, e.g. a thinner island is transformed from a lower cluster. It indicates that each preferred thickness of an island can correspond to an independent transition pathway. We thus accumulated hundreds of transformation events to find out the correlation between a transition pathway and a preferred thickness.

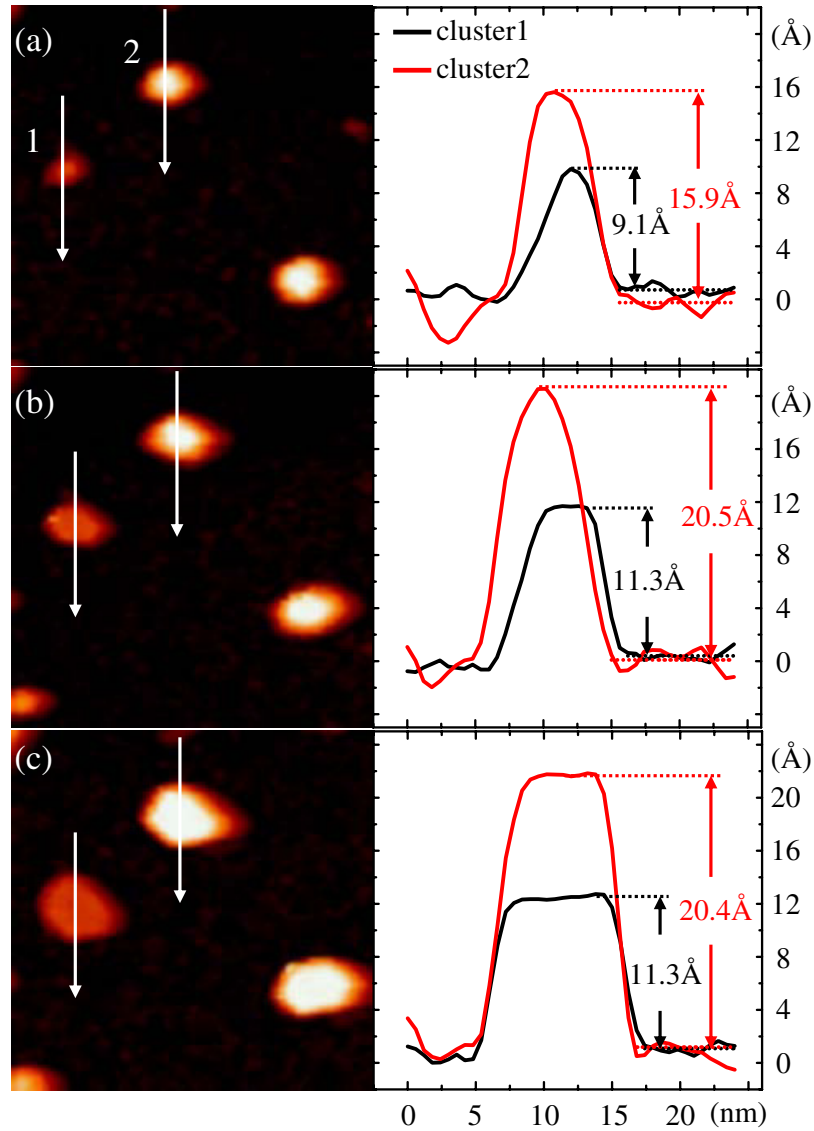


**Figure 3.** *In situ* observations for the growth of two 3D clusters as marked by the numbers in (a). Line profiles at the right side of (a)–(c) represent the morphology evolution of clusters 1 and 2 along arrows in (a). The image size is  $52 \times 52 \text{ nm}^2$ .

**2.2.1. 3D-to-2D growth transition and independent transition pathway.** Figure 4(a) is a statistical result of the heights as a function of the base diameters for the clusters that are not undergoing the growth transition. On average, the height is linearly proportional to the diameter, exhibiting a 3D growth nature. Clusters experiencing the transition are separated in terms of the subsequent island thickness. Figure 4(e) shows the events of clusters finally transforming into 7-layer islands, which is also represented with the height as a function of the diameter for both clusters (cross) and islands (open circle). The diameter of an island can vary from 13 to 24 nm, indicating that once a 7-layer island is formed, it starts to grow in size laterally, exhibiting a 2D growth. We thus conclude that there exists a transition from 3D to 2D in the growth process. This 3D-to-2D growth transition also appears in the formation of 4-, 5-, 6-layer islands, as shown in figures 4(b), (c), (d), respectively.

Lead is known to grow into 3D islands on the  $\text{Si}(111)7 \times 7$  surface at room temperature with the Stranski–Krastanov (SK) growth mode [29]. Although in our case, the growth is

performed at low temperature, after nucleation, the amount of atoms in the nucleus is still too small to establish the QSE strong enough to affect the growth. Therefore, the growth is still dominated by the SK mode, which causes the nucleus to grow into a 3D cluster. Once the aggregated atoms of the cluster are large enough to incite the QSE to overcome the driving force of forming 3D cluster, the 3D-to-2D growth transition occurs. The 3D growth is suppressed and the subsequent growth is in the lateral direction. This causes the Pb islands to have a flat-top surface and to be of a multi-layer thickness. The growth transition reflects interesting information that even a nano-size 3D cluster, its subsequent growth can be affected by the QSE. This does not follow the general concept that the influence of the QSE to the growth can only manifest in the thin film structure as in the growth of  $\text{Ag}/\text{GaAs}(110)$  and  $\text{Ag}/\text{Si}(111)7 \times 7$  [15, 16].

Figure 4(b) shows that right before the transition, the height of the cluster reaches 1.14 nm, which corresponds to four atomic layers in terms of 0.285 nm interlayer spacing.

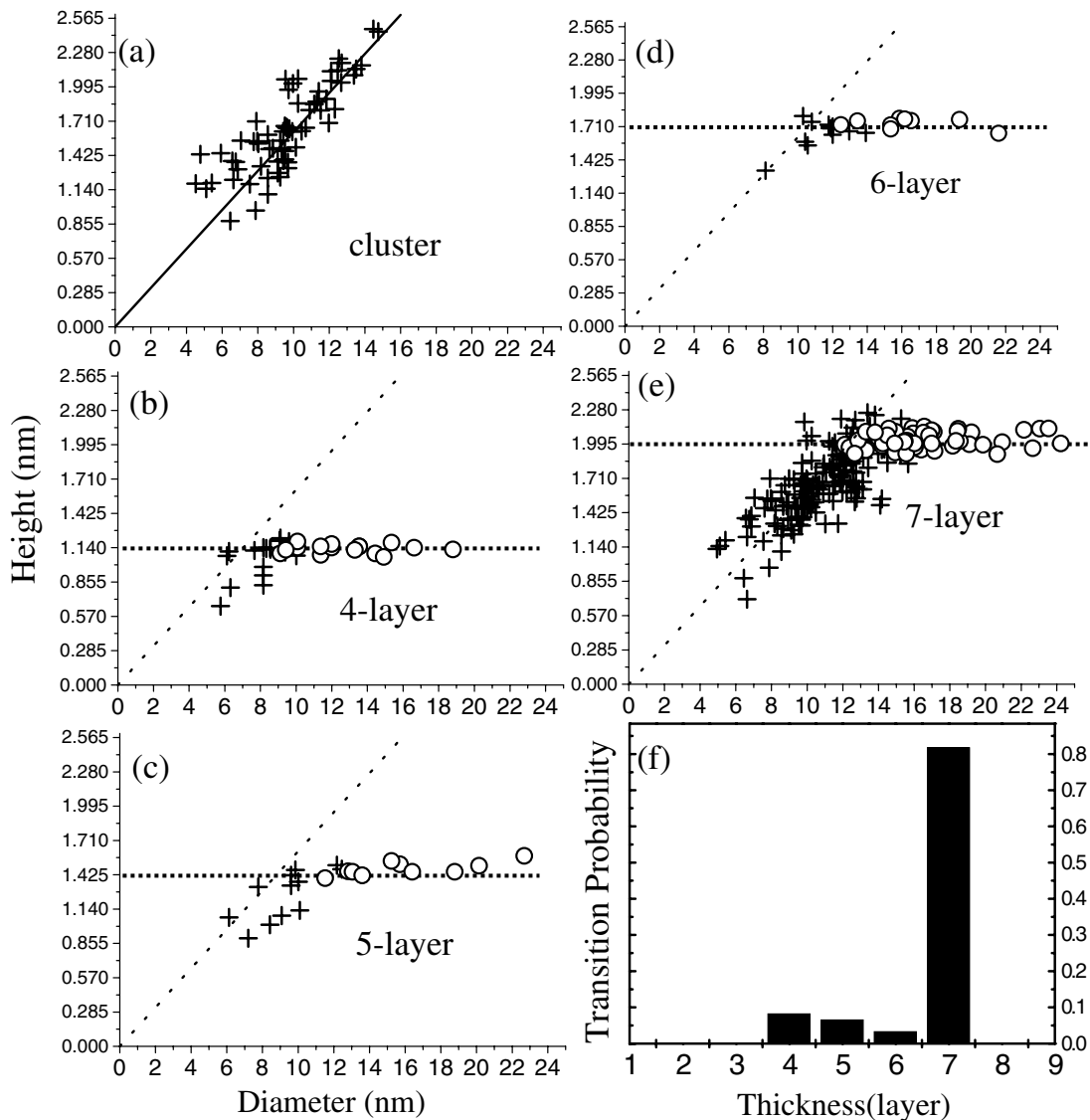


**Figure 4.** (a) A statistic result of the height as a function of the base diameter for clusters without undergoing the growth transition. It can be fitted by a linear line to show the 3D growth of clusters. (b)–(e) Clusters experiencing the transition are separated in terms of the subsequent island thickness, which is also represented with the height as a function of the diameter for both clusters (cross) and islands (open circle). (f) The transition probability of clusters transforming into islands of different thicknesses.

This implies that the cluster is necessary to gain the equivalent height before becoming 4-layer islands. The equivalent heights are also observed in the events of clusters transforming into the 5-, 6-, 7-layer islands as shown in figures 4(c)–(e). We therefore conclude that the transition pathway should be that an  $N$ -layer island is transformed from an  $N$ -layer height cluster. Islands of each thickness thus have a unique growth path. The distribution of cluster heights versus sizes in figures 4(b)–(e) follows a linear dashed line, which is the same as the solid line in figure 4(a), indicating the clusters experiencing the transition are identical to the clusters maintaining 3D growth. The height distribution of clusters in figure 4(a) covers all island thickness, reflecting that the fate of a growing cluster has two choices: one is to follow the transition pathway to become an island; the other is to continue to grow into a higher cluster. Therefore, the transition timing for the formation of a thinner island is earlier than that for forming a thicker

island. The multiple-thickness distribution thus basically manifests a sporadic nature in the timing of the 3D-to-2D transition. Figure 4(f) shows transition probabilities of the clusters transforming into the islands of different thicknesses. The transition probability for 7-layer islands is much larger than those for the islands of other thickness, this is the reason why the 7-layer island is observed to be the most abundant. There is no cluster transforming into the island with thickness below 4-layer, and therefore those kinds of thicknesses are forbidden.

**2.2.2. Temperature effect on island formation.** In contrast to the growth of flat-top Pb islands at low temperature, Pb is grown into 3D islands at room temperature. Therefore, it is interesting to investigate what temperature at which flat islands still can grow. Figure 5 displays the growth of islands at temperatures from 190 to 250 K at a coverage of 3.2 ML. In this

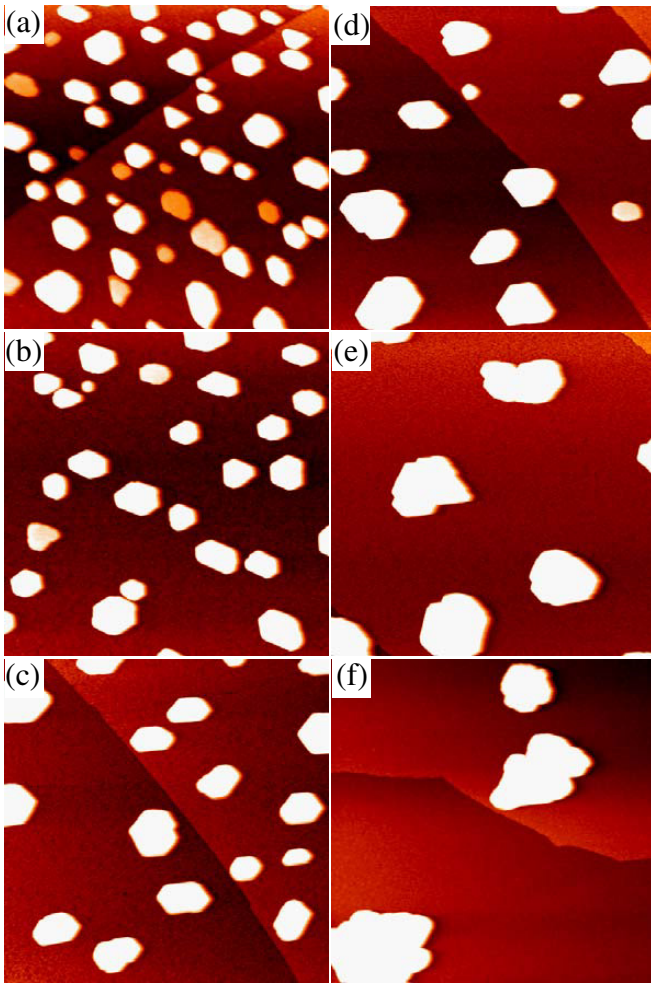


**Figure 5.** The growth of Pb islands at (a) 189 K (b) 198 K (c) 208 K (d) 217 K (e) 226 K and (f) 254 K at a coverage of 3.2 ML. The image size of (a)–(c) is  $300 \times 300 \text{ nm}^2$ , (d) and (e) is  $500 \times 500 \text{ nm}^2$ , (f) is  $1000 \times 1000 \text{ nm}^2$ .

temperature range, the top surface of the islands maintains their atomic flatness. The thickness measurement reveals that the height of Pb islands is still confined in the 4–9 layers range. It indicates that the effect of quantum confinement sustains even when temperature reaches 250 K. As the temperature is raised, the island density decreases, and the island size increases, manifesting a competing process between the island nucleation and growth. The competition arises because Pb adatoms diffuse faster at higher temperature, the probability for an adatom to attach to an existing island instead of nucleating a new island thus increases. According to the nucleation theory, in the low coverage limit with isotropic diffusion, the island density  $N$  is given by [56]

$$N \sim \exp [(i E_d + E_i) / (i + 2) k_B T], \quad (1)$$

where  $E_d$  is the activation energy for diffusion and  $E_i$  is the binding energy for the critical size  $i$ . The Arrhenius plot of the island density versus temperature shows a linear relationship as demonstrated in figure 6. It implies that equation (1) can be applied to describe the growth of Pb islands here. For some homoepitaxy systems in which single-step 2D islands

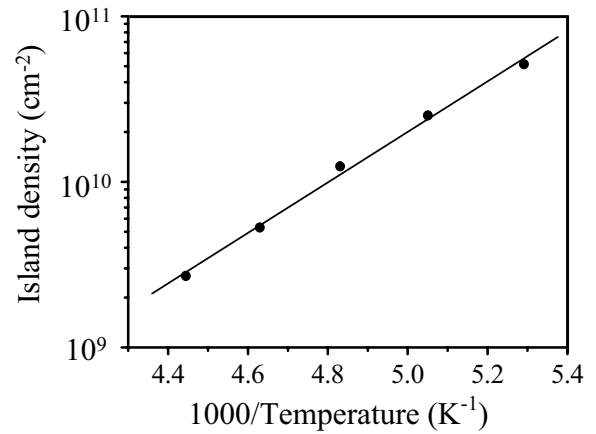


**Figure 6.** The Arrhenius plot of the island density versus temperature, showing a linear relationship.

are formed, the critical size of the nucleation of islands is one or two atoms, depending on the epitaxy temperatures. For example, Stroscio *et al* observed the growth of Fe on the Fe(100) surface [57, 58]. They have found that the critical size  $i$  is one when the growth temperature is below 250 °C. Tsui *et al* studied the nucleation and growth of Rh(1 1 1) [59]. They have found that the critical cluster size of  $i = 1$  below 600 K and  $i = 2$  above 600 K. Since the Pb islands, in our case, are formed on the wetting layer, the nucleation process is supposed to be similar to the homoepitaxy and the critical size should be close to that in the homoepitaxy system. The number of aggregated atoms for manifesting the QSE should be much larger than the critical size. We believe that the nucleation process must occur before the QSE takes place. Thus, the nucleation and the QSE are two independent factors in the formation of an island, the former determines the density of the island and the latter determines the thickness of the created island.

**2.2.3. Critical size of nucleation of island.** Since Pb islands have 2D growth behaviour, another question we ask is whether the growth of multi-layer 2D islands can be described by a 2D theory of growth. To answer this question, we analyse the average island size (area) at different coverages. Figure 7(a) shows the average island size as a function of thickness at the coverage of 0.8 and 1.6 ML above the wetting layer at 208 K. The average size is insensitive to the thickness, indicating the growth rate of the island size is nearly independent of the island thickness. Figure 7(b) demonstrates that the average size of each thickness becomes double when the coverage changes from 0.8 to 1.6 ML, implying islands of any thickness grow in size instead of in thickness, again showing the 2D growth behaviour. Thus, the growth rate of the island volume or the ability of absorbing free atoms of the islands linearly increases with thickness as shown in figure 7(c). This linear relationship is due to the fact that the vertical growth is suppressed after the 3D-to-2D growth transition. The probability that a mobile atom is adsorbed into the multi-step edge of an island is linearly proportional to the island thickness. Since the maximum probability is 1, the linear dependence indicates the absorbed

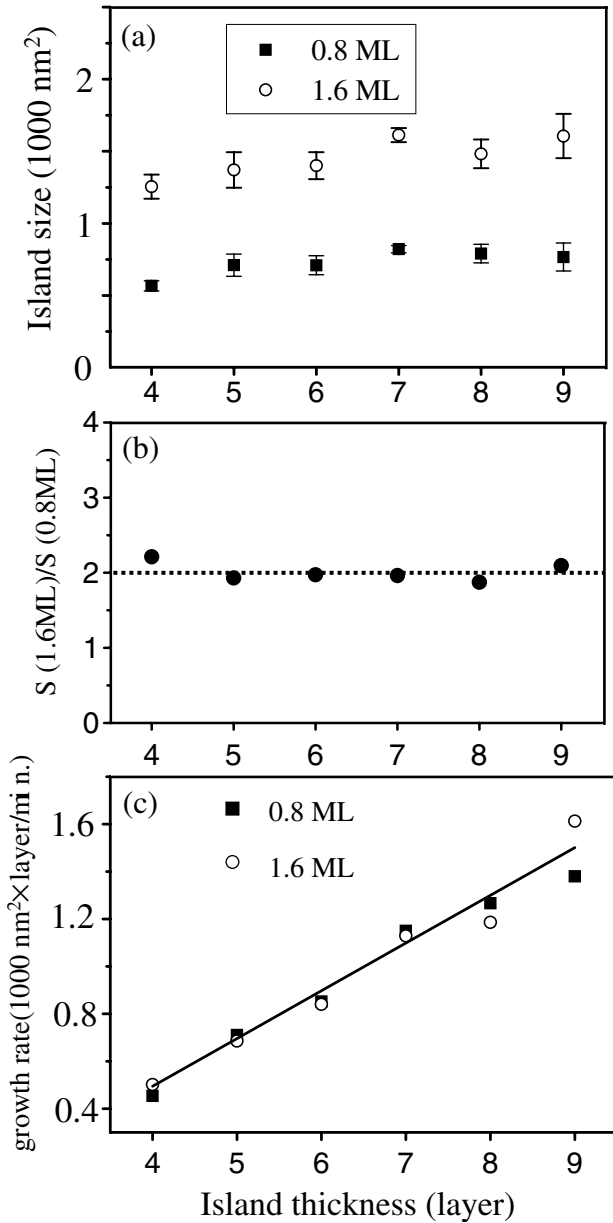


**Figure 7.** (a) The average island size (area) as a function of island thickness at the coverage of 0.8 and 1.6 ML above the wetting layer. (b) The average size of each thickness becomes twice when the coverage changes from 0.8 to 1.6 ML, showing the 2D growth behaviour. (c) The growth rate of island volume as a function of island thickness, showing a linear dependence.

probability should be smaller than 1, which means that the mobile atoms at the island edge have a chance to escape from islands for all kinds of thicknesses. Since the number of absorption site of the island edge is linearly proportional to the thickness, the absorbed probability, thus the growth rate of the island volume, linearly increases with the island thickness. This results in the island size to be insensitive to the thickness. Therefore, the growth of these multi-layer 2D islands should be similar to that of single-layer 2D islands.

The scaling theory [60] has been used to derive the critical size of single-layer islands in homoepitaxy systems. According to this theory, there exists a universal scaling function  $f_i(u)$  which depends only on the critical size  $i$ , and it can

be related to the size distribution of the single-layer island according to

$$f_i(s/S) = Ns(\theta) S^2/\theta, \quad (2)$$

where  $Ns(\theta)$  is the island-size distribution, corresponding to the number density of islands at size  $s$  at covered area  $\theta$  and  $S$  is the average island size. Theoretical scaling functions of different critical sizes are derived from the scaling theory. Using equation (2), one can obtain the experimental scaling data from the island-size distribution. By comparing the theoretical scaling function with the experimental scaling data, the critical size can then be derived.

We have described the growth process after the nucleation; now we further study the critical size of the nucleus. Since Pb islands behave similar to single-layer islands, an interesting question is whether the scaling theory can be used to analyse these multi-layer islands to find their critical size. We pose an argument. Let us assume that there is a size distribution of single-layer islands and it obeys the scaling law of equation (2). If each 1-layer island is folded into a 2-layer island, the size of each island and the average size as well as the covered area, which is the total area of all single-layer islands, would be half of the original ones. The number density of islands would be twice. Therefore, equation (2) for 2-layer islands becomes

$$f_i((s/2)/(S/2)) = 2Ns(\theta) (S/2)^2 / (\theta/2), \quad (3)$$

which, after rearranging equation (3), becomes

$$f_i(s/S) = Ns(\theta) S^2/\theta. \quad (4)$$

Equation (4) returns to the same scaling form, indicating that the scaling theory is still valid for understanding the critical size of multi-layer 2D islands. However, the nucleation has to be independent of the vertical growth mechanism in the formation of a multi-layer island. In some homoepitaxy experiments, the Arrhenius plot of the single-layer island density as a function of temperature always reveals a linear relationship [58, 59], and it also appears in the growth of multi-layer Pb islands as shown in figure 6. This implies that the nucleation of Pb islands should be similar to that of single-layer islands since the Pb islands are created on the Pb wetting layer. We thus apply the scaling theory to investigate the critical size of the Pb islands. As the island size is nearly independent of the island thickness, we analyse the size distribution of all islands without distinguishing their thickness. Figure 8(a) shows the size distribution at the coverage of 0.8 and 1.6 ML. These two distributions can be scaled into two nearly identical distributions by the scaling equation as shown in figure 8(b), showing a similar behaviour as the single-layer islands. The solid curve is the theoretical scaling function of critical size of three atoms [60], and it matches these two groups of the experimental scaling data well. Thus, we conclude the Pb tetramer is the smallest stable nucleus in the incipient growth stage.

Based on the above analysis and observations, we propose a mechanism of formation of multi-layer 2D Pb islands. First, after the completion of the wetting layer, every four Pb atoms form a tetramer as a stable nucleus for the further growth.

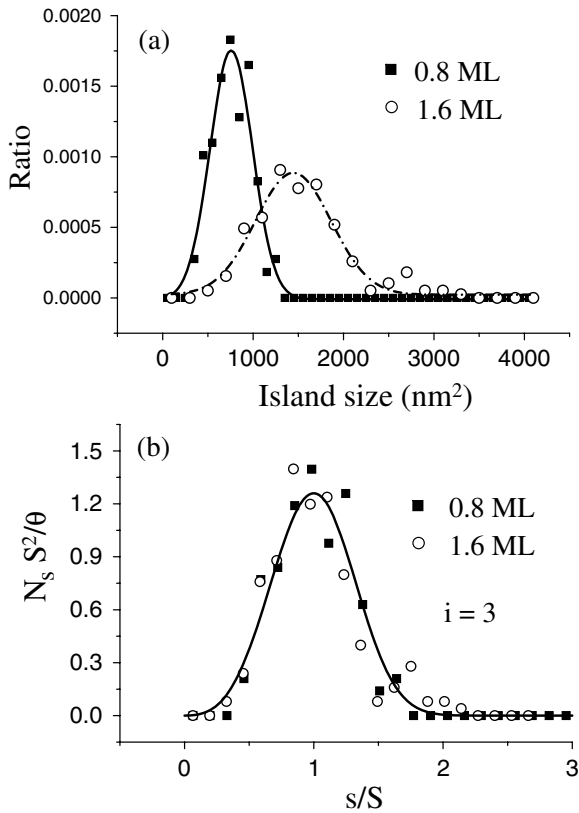


**Figure 8.** (a) Pb island size distributions at the coverage of 0.8 and 1.6 ML above the wetting layer. The solid and dashed–dotted lines are smooth fitting lines to the data points. (b) The two size distributions in (a) can be scaled into nearly identical distributions. The fitting curves of scaling data match the scaling function of critical size of three atoms.

Following the nucleation, SK growth mode provides the initial growth mechanism for forming 3D clusters. When the amount of aggregated atoms of 3D clusters is large enough to establish the QSE to suppress the SK growth, the lateral growth governs the final stage of the formation of a 2D Pb island. Each preferred thickness for 2D island growth corresponds to a unique pathway of the 3D-to-2D growth transition. The energetics is optimum for the QSE when the height of 3D clusters is 7 layers, thus the 7-layer island is most abundant. In addition, our observations show the island size is insensitive to the thickness, thus we can treat multi-layer flat-top Pb islands as single-layer islands and derive their critical size from the scaling theory.

### 2.3. Interface effect

It is well known that the Si(1 1 1)7 × 7 surface can be converted into the 1 × 1 bulk-terminated structure if further annealing is performed after the deposition of Pb on the Si(1 1 1)7 × 7 surface. Pb atoms on the bulk-terminated surface can give rise to several different phases depending on the coverage. For example, incommensurate (IC) phase, 1 × 1 phase mixed with  $\sqrt{3} \times \sqrt{3}$  phase exist at a coverage just above and below 1 ML, respectively [35]. Previous studies have shown that the Schottky-barrier at the Pb/Si(1 1 1)7 × 7 interface is different

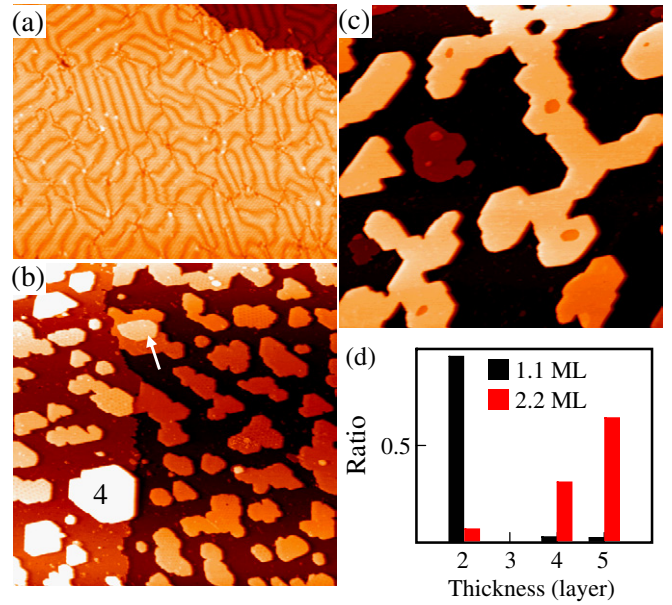


**Figure 9.** (a) The typical topography image of the incommensurate Pb/Si(1 1 1) surface (image size: 100 × 78.5 nm<sup>2</sup>). (b) The growth of flat-top Pb islands on the incommensurate Pb surface after depositing 1.1 ML. At this coverage, there are few 4-layer islands (mark by number) and the 3-layer island is never found but the third layer on some 2-layer islands can be observed (indicated by an arrow). (c) The topography image at coverage of 2.2 ML, showing the island density is reduced and island size becomes large. (d) The ratio distribution as a function of island thickness, showing the preferred thickness is 2 layers at 1.1 ML and the 4 and 5 layers become the next preferred thickness at 2.2 ML. The image size of (b) and (c) is 300 × 300 nm<sup>2</sup>.

from that at the Pb/Si(1 1 1)1 × 1 interface [36], indicating that the charge transfer between Pb and Si for these two interfaces is different. Since the charge transfer at the metal/semiconductor interface is an important factor in the electronic growth of a film, we expect that the Pb growth on the IC phase would be different from that on the Si(1 1 1)7 × 7.

Figure 9(a) shows a typical STM image of the IC Pb surface [35], which consists of domains (bright region) and domain walls (dark region). In a domain, every three Pb atoms gather to form a trimer and the lattice of the trimers displays a periodicity of  $\sqrt{3} \times \sqrt{3}$ . Every two Pb atoms in the domain walls form a dimer. In contrast to the Pb growth on the Si(1 1 1)7 × 7, the islands can be grown on the IC phase directly without an additional wetting layer. Figure 9(b) demonstrates the growth of Pb islands with the (1 1 1) surface on the IC surface after depositing ~1.1 ML of Pb at 208 K. This coverage is measured in terms of the lattice constant of the Pb(1 1 1) surface. The ratio distribution of islands as a function of thickness is plotted in figure 9(d), which reveals that most of islands are of 2 atomic layers in thickness, marking the critical thickness for the growth on this substrate. At this coverage, 4-layer (indicated by number in figure 9(b)) and 5-layer islands are seldom found, and they do not appear at lower coverage. In comparison with the growth on the substrate of the Si(1 1 1)7 × 7 surface, which can have six different kinds of preferred thicknesses, the primary thickness of the grown islands on the IC surface is just of

one kind. It demonstrates that the interface indeed plays an important role in the electronic growth. Figure 9(c) shows that the island density is reduced and the island size becomes larger as the coverage becomes 2.2 ML. The ratio distribution of this coverage shown in figure 9(d) demonstrates that the dominant thickness is 4 and 5 layers, and 2-layer thickness becomes a minor one. Thus 4-layer and 5-layer are the next preferred thickness for growing islands. Recent studies by SPA-LEED have shown that the 5-step islands are the most stable islands [61]. This is consistent with our result at higher coverages. In our observation, the complete 3-layer island is never found and the third layer (indicated by an arrow in figure 9(b)) can only be grown on 2-layer islands of sufficient sizes. Therefore, the 3-layer island is unfavourable for the Pb growth on the IC surface. This is a further distinct behaviour compared with the growth on the Si(1 1 1)7 × 7 surface, in which there is no ‘gap’ in the window of preferred thickness.

#### 2.4. Quantum-well states in Pb islands

Since the creation of Pb islands is a QSE-induced growth phenomenon, one can explore the quantum-well states in islands by using spectroscopy technique in STM. The first observation of the quantum-well states for individual Pb islands grown on the Si(1 1 1) surface was made by Altfeder *et al* [62]. Figure 10(a) displays  $dI/dV$  spectra taken on islands of different thicknesses. The number  $N$  at the right end of each curve represents the number of atomic layers in thickness. In each curve, there are two characteristic peaks as marked by arrows around the Fermi level. The peak separations and positions of some peaks obviously change with the island thickness. These features imply that the peaks are associated with the quantum-well states in islands. According to the infinite-well model, the relation between the energy separation of quantum-well states around the Fermi level and the width is

$$\Delta E = \hbar v_F \pi / H, \quad (5)$$

where  $v_F$  is the Fermi velocity and  $H$  is the width of the quantum well [62]. The inverse of energy separation ( $\Delta E$ ) of the quantum-well states obeys the linear dependence on thickness, which is demonstrated in figure 10(b). The open circles are results of Altfeder *et al* [62] in the thickness range from 8 to 15 layers. Although our observed island’s thicknesses are from 4 to 9 layers, we find our data (solid circles) follow the same linear dependence. The extrapolated  $1/\Delta E$  crosses the height axis at  $-3$ , implying that the actual width for confining electrons needs to be added by 3 layers. Therefore,  $H = (N + 3)d$ , where  $d$  is the interlayer spacing. However, our careful measurement shows that the wetting layer is about 2 ML, indicating that the thickness of a Pb island with respect to the Si substrate is not equal to the width of the infinite well. This is due to the fact that the potential well in the island is finite. The electron can penetrate into each side barrier at the Pb/Si and Pb/vacuum interface because of the wave nature, which is roughly  $d/2$ , and it thus explains  $H = (N + 2 + 1/2 + 1/2)d = (N + 3)d$ .

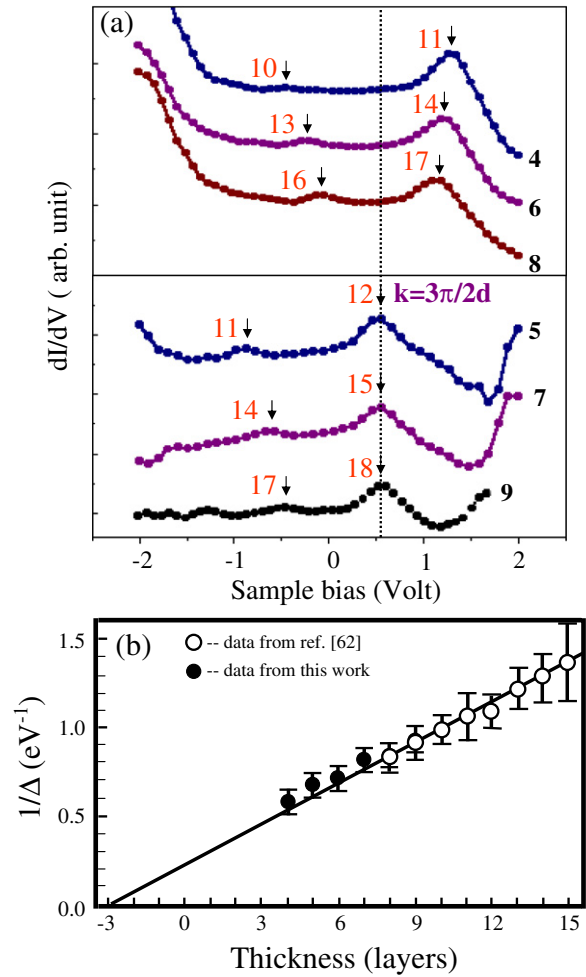


**Figure 10.** (a) Quantum states in the  $dI/dV$  spectra around the Fermi level for different thicknesses of islands. Arrows and numbers at their right side mark the energy levels and the quantum numbers of quantized states, respectively. (b) A duplicate of figure 4 from [62], which shows the inverse of energy separation of adjacent quantum states as a function of thickness of Pb film with respect to the wetting layer. Our results indicated by solid circles can be fit into the linear dependence and overlap the open circles at 8 and 9 layers. (Adapted with permission from [62], copyright 1997, American Physical Society.)

Lead is known to possess a nearly free-electron Fermi surface [63], and therefore electrons in Pb islands can be considered as free electrons being confined between the vacuum and the Pb/Si interface. Although the potential well in the island is finite, figure 10(b) shows that the quantum well states in the island can be realized with the infinite well. The wave vector  $k$  in the infinite well is

$$k = n\pi/H, \quad n = 1, 2, \dots, \quad (6)$$

where  $n$  is the quantum number. In figure 10(a), a quantum-well state in the 5, 7 and 9-layer islands at  $\sim 0.56$  eV above the Fermi level, indicated by a dashed line, is obviously independent of the thickness. This constant state can be inferred from the Fermi level measurement [39, 63], where along the [1 1 1] direction it falls near to  $\pi/2d$  ( $d$  is the interlayer spacing) of the second band in the reduced zone scheme, which is equivalent to  $3\pi/2d$  for the free electron

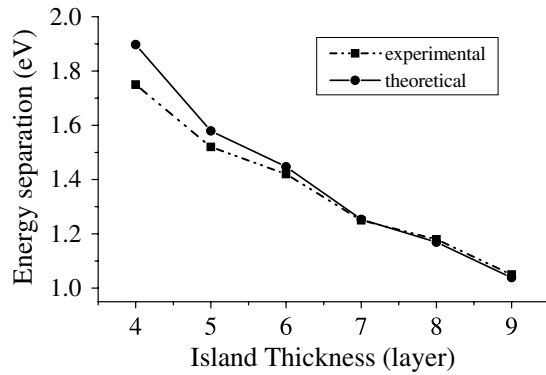


**Figure 11.** Comparison between the measured energy separation in figure 10(a) and the theoretical calculation.

model. Substituting this  $k$  of  $3\pi/2d$  into equation (6) and using  $H = (N + 3)d$ , for 5, 7, 9-layer islands, the corresponding quantum numbers for fixed states can be determined as  $n = 12, 15, 18$ . Other quantum-well states can then be numbered accordingly. In order to examine the validity of those quantum numbers, we calculate the energy separation  $\Delta E$  of adjacent states with the equation

$$\Delta E = \hbar^2 (2n + 1) \pi^2 / 2m^* H^2, \quad (7)$$

where  $m^*$  is the effective mass in the [1 1 1] directions, which is  $1.14m_0$  [41]. The dotted–solid line in figure 11 represents the calculation results. These values agree well with the experimental measurements indicated by the square–dashed line. The calculated data reveal a slight oscillatory aspect, which is also observed in the experimental results. Therefore, a simple infinite potential well model seems sufficient to qualitatively describe the electronic property of a thin Pb film.

### 3. Influence of physical properties of the observed system on the QSE

Since the QSE is investigated in real system, its behaviour is inevitable to be influenced by the physical properties of the system. In this section, we introduce that the QW states, the transmission resonance, and the Gundlach oscillation can be affected by the periodic distortion of the lattice, the electric field in the tunnelling gap, and the surface reconstruction, respectively.

#### 3.1. Strength modulation of quantum-well states in Pb islands with periodic distortion

As we have mentioned in section 2.3, the preferred thickness of Pb islands on the Pb/Si(1 1 1)  $\times$  1 interface is three atomic layers. Previous study has demonstrated that there are two types of periodic pattern on these islands [64]. Recently, low energy electron diffraction (LEED) studies by Hupalo *et al* [65] and theoretical studies by Chan *et al* [66] show that there exists a considerable amount of geometric corrugation induced by the interface relaxation on the surface of such thin Pb films, implying the pattern is a pure geometric structure. We used STM and spectroscopy to study two types of pattern [23]. Our studies demonstrate that there indeed exists the geometric corrugation associated with the interface structure on islands,

consistent with the LEED observation. Nevertheless, our tunnelling spectra also reveal that the strength of QW states in the Pb islands is modulated periodically with the geometric corrugation as well. The strength modulation of the QW states significantly affects the pattern aspect with changing applying bias voltage, indicating that the patterns in STM images are the periodic superposition of geometric corrugation and electronic contribution.

For detecting the electronic contribution in the pattern at different biases, we use  $Z$ – $V$  spectroscopy to probe the electronic structures of Pb islands. In the  $Z$ – $V$  measurement, the tip trajectory was recorded with an active feedback, while the sample bias was ramped from 0.2 to 2 V or from  $-0.2$  to  $-2$  V. To obtain the differentiation of spectra, a lock-in amplifier was applied, and a dither voltage of 30 mV at a frequency of 5 kHz was added to the sample bias. The frequency is too high for the feedback loop to react, and therefore the output quantity from the lock-in amplifier is  $dI/dV$ . It does not correspond to  $dZ/dV$  but it can be representative of  $dZ/dV$ . During the acquisition of a  $Z$ – $V$  spectrum, the signal from the lock-in amplifier is recorded simultaneously to obtain a spectrum similar to the  $dZ/dV$ – $V$  curve. This lock-in technique was used to obtain the mapping of spectral intensity as well.

Figure 12(a) shows a typical topographic image of grown Pb islands with thickness of three atomic layers on top of the Si(1 1 1) surface, taken at a sample bias of 0.2 V. There appear two types of pattern marked I and II [64] on these islands. Figures 12(b) and (c) display the zoom-in images of type-I and type-II patterns, respectively. It is obvious that type-I pattern is a close-packed structure whereas type-II pattern is a honeycomb-like structure. Both patterns have the same wavelength of 38.4 Å. Since the Pb island is crystallized and has a well-defined (1 1 1) surface, these patterns are most likely originated from the lattice mismatch between the bottom Pb layer (3.5 Å) and Si substrate (3.84 Å), creating a moiré pattern as illustrated in figure 12(d). Green and red solid circles in figure 12(d) represent the atoms at the outer and the second Si layers. Black open circles represent the first layer Pb atoms and those solid ones mark the periphery Pb atoms, outlining a unit cell of the moiré pattern. It is conceivable that this moiré pattern at the bottom layer of a Pb island can manifest itself onto its top surface. Previous studies have shown that the interface relaxation is the mechanism to transfer this moiré pattern [65, 66]. It causes the bottom Pb layer to be corrugated and naturally the top layers to follow suit. However, tunnelling spectroscopy studies also done by Hupalo *et al* reveal that the pattern observed using STM is not a pure geometric corrugation but involves an electronic contribution [65]. According to the principle of STM, a possible way to approach the geometric structure of a Pb surface in this case is to use a low bias in order to avoid the influence of the quantum well states at the higher energies<sup>1</sup>. Two types of patterns in figures 12(b) and (c) were acquired at a low sample

<sup>1</sup> We did not detect any prominent localized states near the Fermi level in  $I$ – $V$  spectra for the Pb film. Therefore, the small range of integration of the density of states for the topography image should approximate the true geometric surface structure.

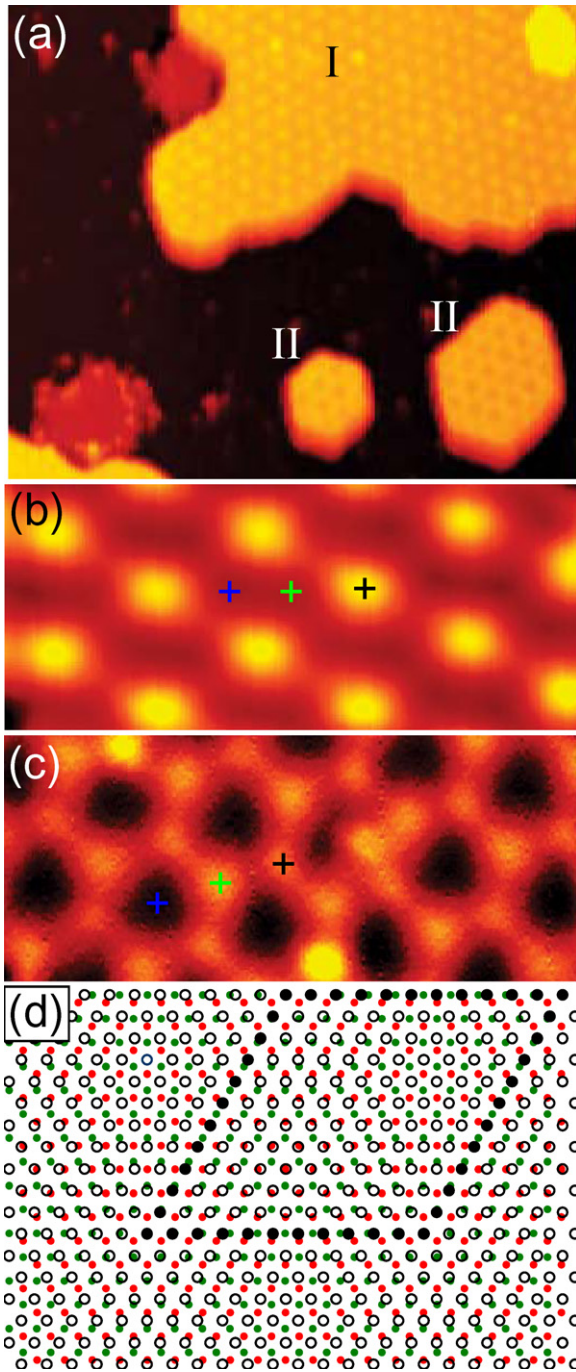


**Figure 12.** (a) Growth of 3-layer Pb islands with types of pattern marked I, II on the IC phase Pb/Si(1 1 1) surface. Image size is  $890 \times 740 \text{ \AA}^2$ . (b) Zoom-in image of type-I pattern and (c) type-II pattern. Image size of (b) and (c) is  $185 \times 77 \text{ \AA}^2$ . Crosses mark positions where tunnelling spectra are acquired. (a), (b), (c) were taken at a sample bias of 0.2 V. (d) Model for producing a moiré pattern with one layer of Pb on Si(1 1 1).

bias of 0.2 V. Therefore, these two patterns can represent the geometric corrugation and we will show additional evidence to confirm this point later. The appearance of two types of geometric patterns indicates that the interface can choose two ways to relax. Owing to the interface relaxation, the structure of the island is periodically distorted. It would be interesting to investigate whether the QW states in islands are influenced

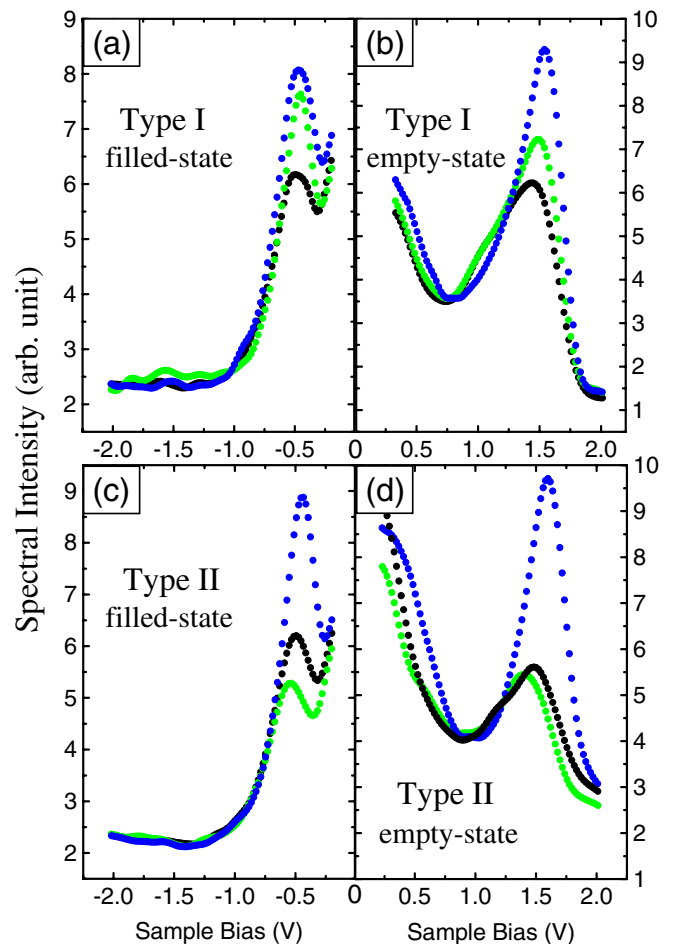


**Figure 13.** The  $dZ/dV$  spectra acquired using lock-in technique on type-I and type-II patterns for (a) and (b) filled state, (c) and (d) empty state. Colours of the spectra correspond to those of crosses in figures 12(b) and (c).

because of this structural distortion. For addressing this issue, we acquire  $Z-V$  spectra at three positions of high symmetry: the unit cell corner and the gravity centres of two triangular halves of a unit cell for both types of patterns, as marked by black, green and blue crosses, respectively, in figures 12(b) and (c).

Figure 13 shows  $dZ/dV$  spectra acquired using the lock-in technique for filled and empty states. The colours of the spectra correspond to those of crosses in figures 12(b) and (c). We can observe one peak of the QW state in each filled state and empty state for all acquired positions on both types of pattern. However, the strength, i.e. the peak height of the QW state, changes with the acquired position, and the sequence of the strengths in filled state is the same as that in empty state. Therefore, our observation reveals that the lattice distortion in Pb islands indeed significantly affects the strength of the QW state. In order to examine whether the strength is modulated with the periodicity of geometric corrugation, we use the lock-in technique to take the  $dZ/dV$  spectral mappings. Figures 14(a) and (b) show, respectively, the STM image of type-I pattern at sample bias of  $-0.2 \text{ V}$  and the  $dZ/dV$  spectral mapping acquired simultaneously. It can be seen that the pattern in figure 14(a) is almost the

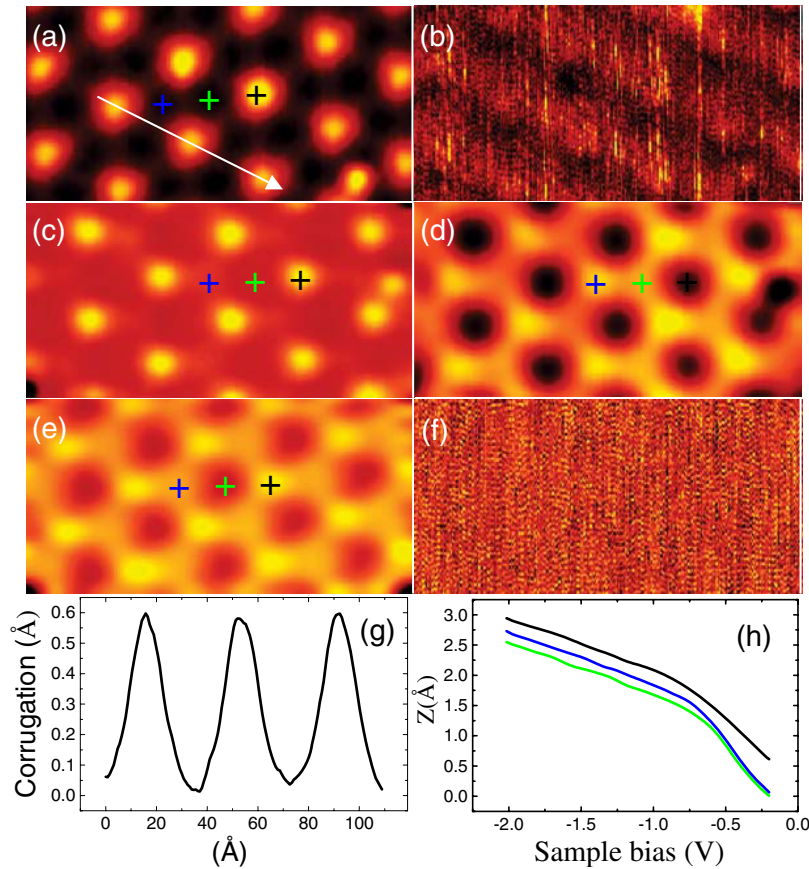


**Figure 14.** (a), (c), (e) STM images of type-I patterns at sample bias of  $-0.2$  V,  $-0.5$  V,  $-2$  V, respectively. (b), (d), (f) Corresponding  $dZ/dV$  spectral mappings of images (a), (c), (e), respectively. All image sizes are  $185 \times 77 \text{ \AA}^2$ . (g) The line profile across the pattern in (a), indicated by an arrow. (h) Corresponding  $Z$ - $V$  spectra acquired at crosses.

same as that in figure 12(b) although the polarity of the bias is reversed. In addition, although the spectral mapping in figure 14(b) shows some contrast, it does not reveal the same two-dimensional periodicity as the STM image in figure 14(a). Therefore, the influence of the electronic contribution at this energy (0.2 eV below Fermi level) is minor, and the pattern in figure 14(a) mainly represents the geometric corrugation. In a similar way, it implies that type-I and -II patterns in figures 12(b) and (c) are the images of geometric corrugation as well (not shown). Figure 14(g) shows the line profile across the pattern in figure 14(a), indicated by an arrow, revealing the corrugation of the pattern. It can be seen from the line profile that the corrugation is about  $0.55 \text{ \AA}$ , which is consistent with  $0.48 \text{ \AA}$  of the LEED measurement and  $0.42 \text{ \AA}$  of the theoretical calculation [65]. When the bias is changed to  $-0.5$  V, type-I pattern as shown in figure 14(c) is nearly the same but the corresponding  $dZ/dV$  spectral mapping shown in figure 14(d) shows a periodic distribution with the same wavelength of the pattern. This bias is close to that of the maxima in the spectra displayed in figure 13(a). In terms of the coloured cross positions in figures 14(c) and (d), the contrast of this spectral mapping accurately reflects the strength sequence in figure 13(a) (brighter regions mean larger spectral intensities). This spectral mapping demonstrates that the strength of the QW state is indeed modulated with the geometric corrugation. Due to the strength modulation of the QW state, the IDOS is inhomogeneous, which further results in the tip being unable

to follow the geometric corrugation during scanning. In terms of the spectra in figure 13(a), the IDOS from  $-0.2$  to  $-0.5$  eV (below the Fermi level) at the position of the blue cross is larger than that at the green cross, which can be attributed to the strength difference of the QW state at these two positions. This inhomogeneous IDOS makes the height at the blue cross, in the topography image of figure 14(c), slightly higher than that at the green cross. This height difference is made larger in figure 14(e) when the bias is changed to  $-2$  V because the IDOS is extended over the complete QW state. Due to this electronic contribution, the type-I pattern in figure 14(e) becomes different from that in figure 14(a). This implies that the pattern in figure 14(e) observed at a high bias of  $-2$  V cannot represent the surface geometric corrugation although there is no contrast in its corresponding spectral mapping shown in figure 14(f). Figure 14(h) shows corresponding  $Z$ - $V$  spectra. All spectra show that the tip height is increased with increasing bias, which results from the increment of the IDOS. Because of the inhomogeneous IDOS, however, the spectra are not in parallel to each other and the relative heights of the tip at  $-0.2$  V are different from those at  $-2$  V. Therefore, it is clear to see that the small height difference between the blue and green crosses at  $-0.2$  V is amplified at  $-2$  V, in agreement with figures 14(a) and (e).

In figure 14(e), the measured height at the position of the black cross is still the highest one in the pattern even though the IDOS is the smallest there (referring to figure 13(a)).

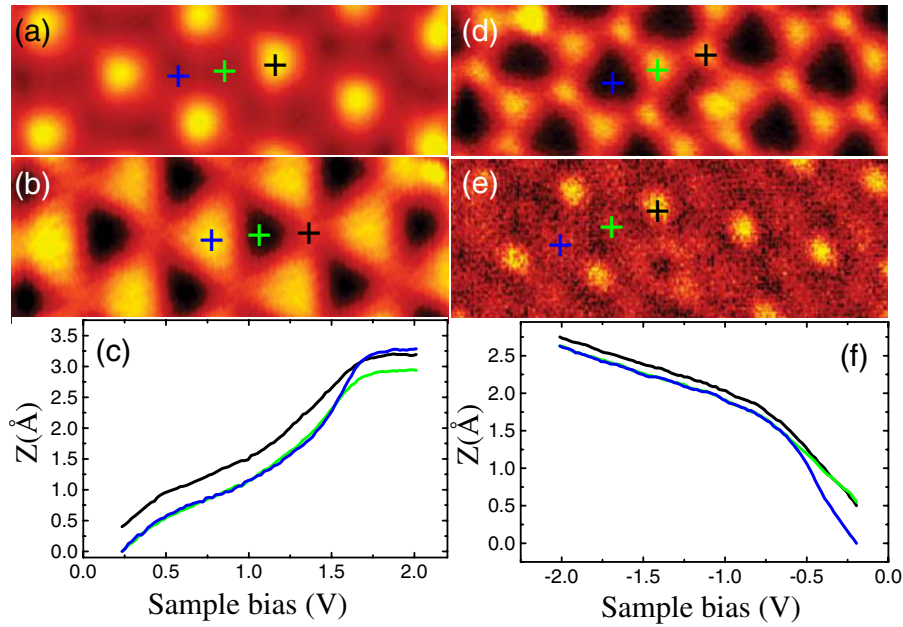


**Figure 15.** (a), (b) Type-I pattern at sample bias of 0.2 and 2 V. (c) Corresponding  $Z$ - $V$  spectra acquired at crosses in (a). (d), (e) Type-II pattern at sample bias of  $-0.2$  and  $-2$  V. (f) Corresponding  $Z$ - $V$  spectra acquired at crosses in (d). All image sizes are  $185 \times 77 \text{ \AA}^2$ .

This indicates that the electronic contribution is not strong enough to alter the pattern of the pure geometric corrugation. However, the change can happen as the pattern is observed in the empty states. Figures 15(a) and (b) show type-I patterns at 0.2 V and 2 V, respectively. In figure 15(b), the height at the blue cross becomes higher than that at the black cross and the whole pattern is transformed into a close-packed structure of triangles, different from the purely geometric corrugation in figure 15(a). This change can be realized from the spectra in figure 13(b), in which the IDOS for a complete QW state in the blue curve is larger than that in the black curve. The difference is large enough to overcome the geometric variation between the black and blue crosses. The contrast at these two locations is thus reversed. Figure 15(c) shows the corresponding  $Z$ - $V$  spectra, and it can be seen that the blue curve crosses over the black curve, exhibiting the occurrence of the contrast reversal. This alternation also occurs in type-II pattern. Figure 15(d) shows the type-II pattern at  $-0.2$  V, representing the geometric topography. However, this honeycomb-like pattern is transformed into a close-packed pattern similar to the type-I pattern in figure 15(a) as the bias is changed to  $-2$  V (figure 15(e)). Referring to the strength of the QW states shown in figure 13(c), the height difference between the green and the blue crosses in figure 15(d) is totally compensated in figure 15(e) by the electronic contribution, and only the circular corrugation around the black cross is left in the type-II pattern. This height compensation is consistent with the corresponding  $Z$ - $V$  spectra shown in figure 15(f), in which the blue curve overlaps with the green curve when the bias is beyond  $-1$  V.

Spectra in figure 13 reveal a consistent behaviour that the larger strength of the QW state corresponds to the lower position in the geometric corrugation, and vice versa. This behaviour leads us to propose a qualitative explanation for the phenomenon of the strength modulation of the QW state.

Since the geometric corrugation originates from the interface relaxation, Pb islands have the periodic distortion, a wave-like structure. Consequently, the ion cores with positive charge near the higher region are subject to tensile stress whereas those around the lower region are subject to compressive stress. The tensile stress pulls ion cores away from each other but the compressive stress pushes them close to each other. In order to maintain the local electric neutrality, electrons are induced to screen these nonuniform positive charges [67]. The electron density in the region with compressive stress should thus be higher than that at the region with tensile stress, creating the inhomogeneous DOS in the islands. Since the electronic structure of a Pb island consists mainly of QW states and each of them forms a subband, an inhomogeneous DOS is naturally reflected in a strength variation of the QW states. Therefore, the strength modulation of QW states is a manifestation of the electronic screening effect induced by the lattice distortion.

It can be expected that with increasing thickness, the geometric corrugation induced by the interface relaxation would weaken and therefore the strength modulation of the QW states would fade out. The pattern from the interface structure is supposed to disappear on the surface of a thick film. However, previous STM study on a Pb film with a thickness of 5 nm has demonstrated that the pattern can still be observed even though the strength of the QW state is spatially uniform [68]. In this case, the mechanism for forming pattern is the phase variation of the QW states at the interface, different from that in the case of thinner films.

### 3.2. Transmission resonance shifted by electric field in tunnelling gap

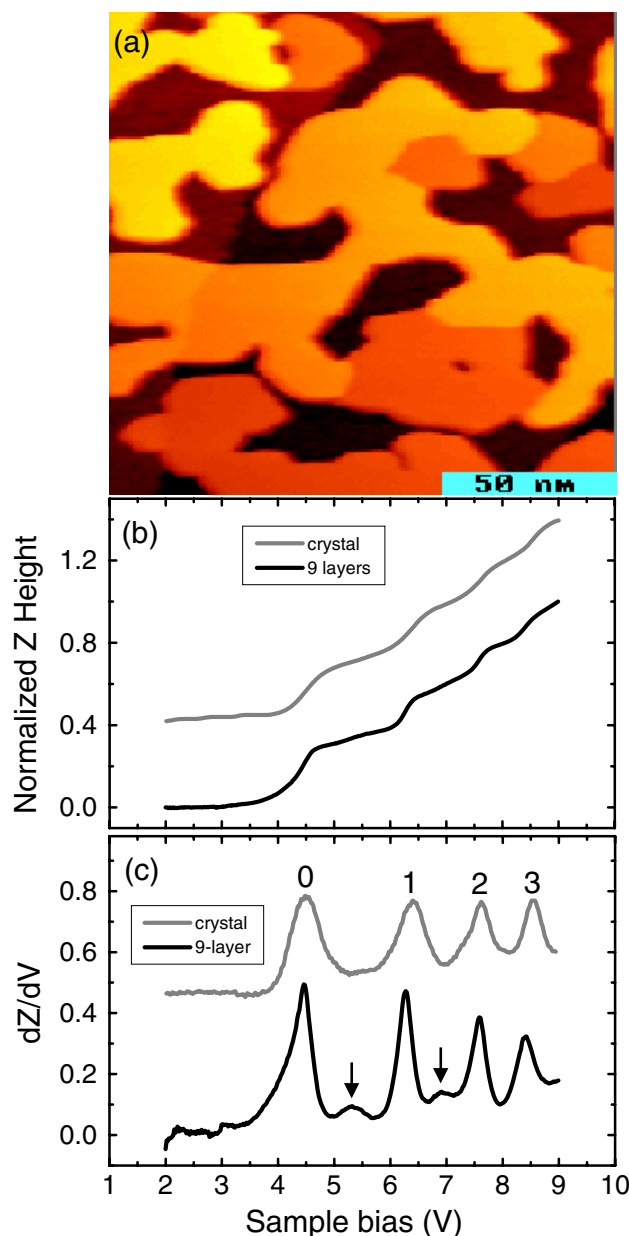
**3.2.1. Transmission resonance.** Transmission resonance is a quantum phenomenon of the free electron scattered by a one-dimensional potential well in the metal film, i.e. the QSE above

the vacuum level. It originates from the interference of the electron waves, which are reflected from the film surface and the film–substrate interface. Electrons with energy matching levels of the transmission resonance can, in principle, transmit the well without suffering any reflection loss [69]. In the real systems, transmission resonance can be observed by the low energy electron transmission spectroscopy (LEETS) [6] for some free-electron-like metal films such as Ag and Cu films [7, 8]. These previous studies clearly demonstrate a common feature, i.e. when the film thickness increases, the energy levels of transmission resonances prominently shift towards the vacuum level and the separation between them reduces subsequently. This thickness-dependent trend agrees with the prediction of the quantum theory.

The first observation of transmission resonance was reported by Kubby *et al* on the  $\sqrt{3} \times \sqrt{3}$  Sn/Si(1 1 1) surface [11] using  $Z$ – $V$  spectroscopy combined with the lock-in technique. However, one cannot unambiguously conclude that their observation is of transmission resonance because there was no report of thickness-dependent behaviour. We used  $Z$ – $V$  spectroscopy to probe the electronic structure, above the vacuum level, of the Ag film grown on the Si(1 1 1)  $7 \times 7$  surface [24]. We also observe the signal which is similar to that observed by Kubby *et al*. The energy level of this signal significantly moves towards the vacuum level with increasing film thickness. When the film is thick enough, the signal can occur twice in the biasing voltage range and the energy separation between them decreases with increasing thickness. This thickness-dependent behaviour is consistent with previous studies using LEETS [7, 8]. We thus confirm that the transmission resonance can be probed by  $Z$ – $V$  spectroscopy in STM.

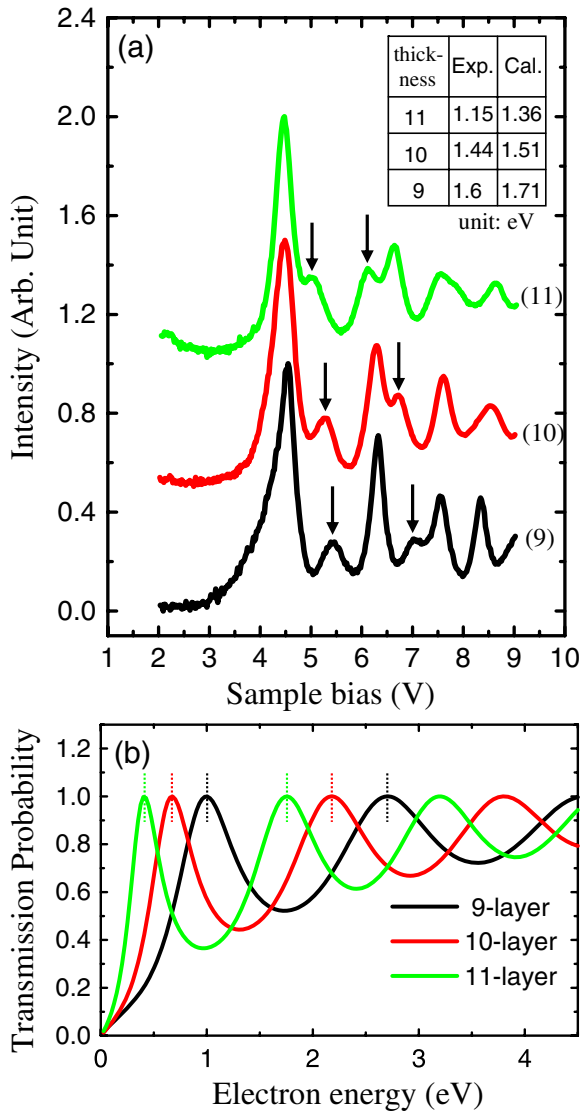
For this experiment a Si(1 1 1)  $7 \times 7$  surface was obtained by annealing the sample to 1200 °C and then slowly cooling it to room temperature. Silver was deposited onto the Si(1 1 1)  $7 \times 7$  surface at room temperature with a flux of 0.26 ML min<sup>−1</sup>. The vacuum was kept below  $2 \times 10^{-10}$  Torr during deposition. After deposition, the sample was transferred to a home-built STM in which the sample was cooled to 109 K. The electronic structures of the Ag films were probed using  $Z$ – $V$  spectroscopy. In the  $Z$ – $V$  measurement, the tip trajectory was recorded with an active feedback, while the sample bias was ramped from 2 to 9 V. A modulation of the sample voltage of 30 mV at a frequency of 5 kHz is added to the sample bias for differentiating the spectrum and taking the spectral mapping.

Figure 16(a) shows a typical STM topography image of an Ag film prepared at room temperature with a coverage of 3.6 ML. At this coverage, about 0.35 ML of Ag were consumed to wet the Si(1 1 1)  $7 \times 7$  surface and the rest grew into flat films with the (1 1 1) face [18]. The growth is not layer-by-layer; thus, several film thicknesses can often coexist. Film thickness can be accurately determined by measuring the height of the film against the exposed wetting layer. The  $Z$ – $V$  spectra were taken on films of different thicknesses. The black curve in figure 16(b) shows such a spectrum, taken on a film of nine atomic layers above the silicon substrate. For comparison, the spectrum is also acquired on the (1 1 1) surface of an Ag crystal,



**Figure 16.** (a) The growth of flat Ag films on the Si(1 1 1)  $7 \times 7$  surface at room temperature at the coverage of 3.6 ML. Image size is  $150 \times 150$  nm<sup>2</sup>. (b)  $Z$ – $V$  spectra measured on the 9-layer thick Ag film (black curve) and crystal Ag(1 1 1) surface (grey curve). (c)  $dZ/dV$ – $V$  curves directly differentiated from the  $Z$ – $V$  spectra in (b).

drawn as the grey curve in figure 16(b). Both curves are similar and reveal step-like features that signify the field emission resonance through the standing-wave states between the tip and sample [12–14]. After numerical differentiation, step-like features become a series of sharp peaks (marked by number) and the spectrum reveals an oscillatory aspect, as shown in figure 16(c), which is known as the Gundlach oscillation. Besides the peaks of Gundlach oscillation, two additional bumps marked by downward arrows are observed in the curve associated with the film. However, these do not appear in the spectrum of the Ag crystal, indicating that the bump feature is specific to the Ag thin films. Figure 17(a) displays the differential spectra obtained by the lock-in technique, with the



**Figure 17.** (a) Spectra acquired on 9–11-layer thick films by lock-in technique with the feedback kept active. Numbers in parentheses indicate film thickness. (b) Calculated curves of transmission probability as a function of electron energy for 9–11-layer thick films. Dashed lines indicate energy levels of transmission resonance.

active feedback on the films containing 9–11 atomic layers (indicated by the number in parenthesis). There, arrows mark the bump features appearing in the curves of different films, and it is obvious that the energy separations between the bump features as well as their energy levels both reduce with increasing film thickness. These characteristics guide us to consider that the bump signals originate from the QSE above the vacuum level (referring to the work function of the Ag film on Si(1 1 1) being 4.41 eV [70]). They derive from the electron waves scattered by a potential well.

According to quantum mechanics, the probability for a free electron being transmitted through a square potential well obeys the following equation [69]:

$$1/T = 1 + V^2 \sin^2(kt) / 4E(E + V), \quad (8)$$

where  $T$  is the transmission probability,  $E$  is the energy of the incident electron,  $V$  is the depth of the potential well,  $t$  is the

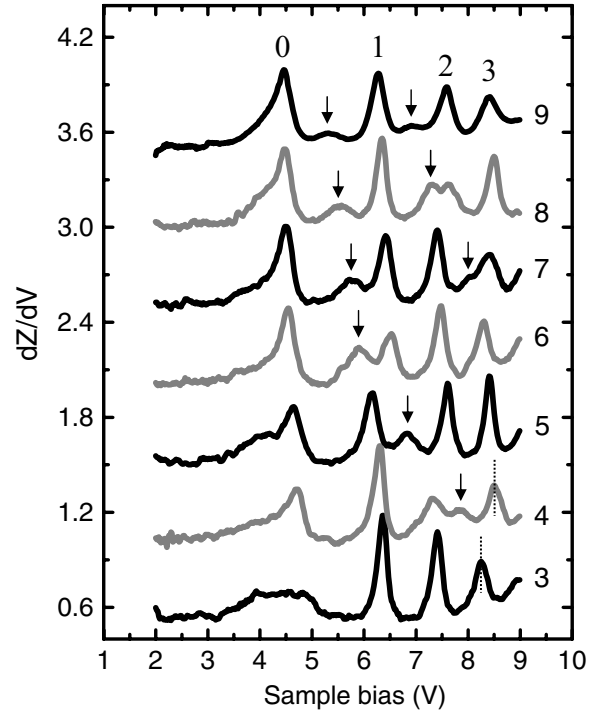


**Figure 18.** Spectra acquired on 3–9-layer films. Numbers at the right-hand side of spectra mark atomic layers of the thickness. Arrows mark the positions of the transmission resonance. Numbers at the top mark the standing-wave states in the spectrum of each thickness.

width of the well,  $k$  is the wave vector of electrons in the well and

$$\hbar^2 k^2 / 2m = E + V. \quad (9)$$

It is obvious that the  $T$  can be one when  $kt$  is equal to an integral multiple of  $\pi$ . At this condition, electrons can penetrate the film completely. This quantum phenomenon is termed the transmission resonance. In the current system, the thin Ag film grown on the Si substrate acts like a potential well to the electrons emitted from the tip. Figure 17(b) shows calculated curves of transmission probability as a function of electron energy for the films of 9–11 layers using equation (1). The bulk values for Ag crystal are adapted here, i.e. the inner potential of 8 eV [7] for  $V$  and 2.5 Å for interlayer spacing along the (1 1 1) direction. Each calculated curve exhibits an oscillatory aspect, indicating that in general electrons can be transmitted and reflected at the potential well with different weighted probabilities. Nevertheless, at some specific energy levels (marked by dashed lines) electrons can penetrate the film completely, resulting in transmission resonance. The energy levels of transmission resonance move towards the vacuum level with increasing film thickness. This is consistent with the bump features shown in figure 17(a). The calculated (Cal.) values of the energy separation between the first two transmission resonances are tabulated in figure 17(a)—these values decrease with increasing film thickness and qualitatively agree with the experimental (Exp.) measurements. It can thus be concluded that the bump features result from transmission resonance.

Figure 18 shows the  $dZ/dV-V$  spectra acquired on films with 3–9 layers. The number at the right-hand side of

each curve denotes the film thickness. In each spectrum there appears four Gundlach oscillation peaks, marked by numbers, and one transmission resonance bump, marked by an arrow. Beyond a film thickness of six atomic layers a second transmission resonance begins to be observed. In some circumstances it is difficult to differentiate the bump from the peaks; for instance, the spectral intensities of both peak 2 and the transmission resonance are about the same in the spectrum of the 8-layer film. However, the peak position of the Gundlach oscillation can be adjusted by tuning the tunnelling current [71], and in this way, the quick alteration in the position and the peak intensity of the Gundlach oscillation can be spotted and thus the transmission resonance bump can immediately be identified. The thickness-dependent behaviour shown in figure 18 is consistent with that of figure 17(a), i.e. as film thickness increases, the energy levels of transmission resonance move towards the vacuum level and their separation decreases. By comparing the intensity distribution of each spectrum, it is obvious that each one is of a unique aspect. The factors for forming these characteristic spectra are the following. First, the transmission resonance moves towards the vacuum level with increasing film thickness. Furthermore, in the spectra of films of 7–9 layers, another transmission resonance of higher energy has revealed. Secondly, there are four Gundlach oscillation peaks in each spectrum. However, the intensity of each peak is not always much higher than that of the transmission resonance as the situation in the spectrum of 9-layer thick film. For example, the intensity of peak 2 in the spectrum of 8-layer thick film is obviously much smaller than those of other peaks but is comparable to that of the transmission resonance. In our observation, this is because the intensity of the standing-wave state would decrease with decreasing separation between it and the transmission resonance. Thirdly, Kubby *et al* has demonstrated that the appearance of the transmission resonance can displace the higher order peak of the Gundlach oscillation to higher energy [11], which also appears in our spectra. For example, because of the appearance of the transmission resonance in the spectrum of the 4-layer thick film, the energy level of peak 3 is higher than that in the spectrum of the 3-layer thick film, as marked by dashed lines. These factors influence the distribution of spectral intensity, rendering figure 18 to be used as a database of the fingerprints for determining the film thickness [72]. Therefore, besides measuring the film thickness directly from height distribution of STM images, one can also distinguish the thickness by acquiring the  $dZ/dV$ - $V$  spectra on films and compare them with the spectra in the database. This is especially useful for Ag films covering the entire wetting layer. Previous studies have shown that Ag can be grown into a complete film on Si(111) $7 \times 7$  by low temperature deposition followed by annealing to room temperature [16]. Figure 19(a) shows an STM image of the Ag film formed by this way. Using STM, we can only determine that the height difference between the light grey and the dark grey region is one atomic layer, but cannot determine the absolute thickness of both regions above the substrate. The black and grey curves in figure 19(b) are the spectra acquired on the dark grey and light grey regions, respectively. From a

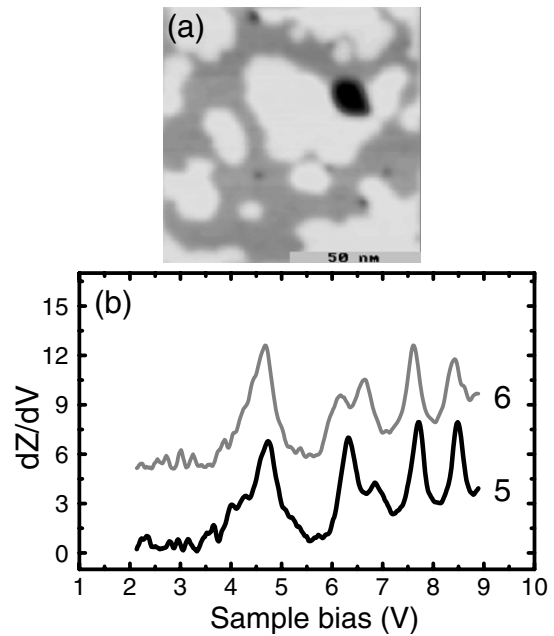


**Figure 19.** (a) Typical STM image of atomic-scale flat Ag films grown on Si(111) $7 \times 7$  at 110 K at the coverage of 5.5 ML followed annealing to RT. Image size is  $1000 \times 1000 \text{ \AA}$ . (b) Grey and black curves are spectra acquired on light grey and dark grey regions in (a), respectively.

comparison with those spectra of figure 18, it is easy to tell that the black and grey curves are the spectra of the 5-layer and the 6-layer thick film, respectively. The thickness of the dark grey and light grey regions can thus be unambiguously identified. Though the spectra exhibit the thickness-dependent behaviour, actually their aspects can be tuned by adjusting the tunnelling current, i.e. the electric field between the tip and the sample. The main alteration in the spectra is that the number of Gundlach oscillation peaks varies with the electric field. In addition, the acquired spectra by different tips may not be alike at the same tunnelling current. In our observation, however, the spectra always can be tuned to be almost identical to that of figure 18 at the criterion of appearance of four Gundlach oscillation peaks. Therefore, the function of identifying film thickness by the spectra can still be preserved.

**3.2.2. Electric field effect.** Recently, Limot *et al* presented  $dI/dV$  measurements on surface-state binding energy and concluded that the surface state can be shifted by the electric field between the tip and the sample [73]. This observation motivates us to infer that the electric field may, likewise, shift the levels of transmission resonance. Our experimental results demonstrate that the transmission resonance indeed can be displaced to higher energy with increasing electric field [25]. To explain this phenomenon, we introduce a field-induced phase variation in the quantization rule, and the calculated results show that the shifting of the transmission resonance agrees qualitatively with experimental observation. In addition, the calculation also predicts that beyond a critical field, the transmission resonance may drop discontinuously to lower energy. This abrupt change has been observed in our system as well.

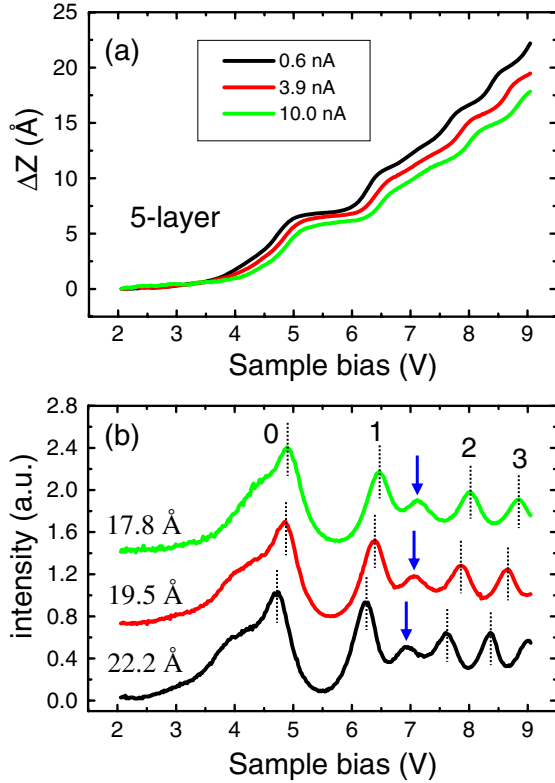


**Figure 20.** (a) The  $Z$ - $V$  spectra acquired on the 5-layer film at different currents. (b) Spectra obtained by lock-in technique, and each spectrum, depending on colour, is acquired simultaneously with each  $Z$ - $V$  spectrum in (a). Arrows and dashed lines mark the energy levels of the transmission resonance and standing-wave states, respectively.

Figure 20(a) shows the  $Z$ - $V$  spectra acquired on the 5-layer film under various set tunnelling currents. It is clear that spectra begin to split up when the sample bias  $V$  exceeds 3.5 V, indicating that the electron tunnelling starts to enter the field-emission regime after this bias. The splitting of the spectra is due to the fact that the feedback system has to control a smaller tip-sample distance to establish a stronger electric field for emitting a larger field-emission current from tip, and vice versa. Therefore, the withdrawn distance  $\Delta Z$  of the tip decreases with increasing current at the same bias, as shown in figure 20(a). Figure 20(b) displays the spectra obtained by the lock-in technique, and each spectrum, depending on colours, is acquired simultaneously with each  $Z$ - $V$  spectrum in figure 20(a). In each spectrum, we can observe four peaks of Gundlach oscillation in the tunnelling gap marked by numbers and one transmission resonance indicated by an arrow. Since the electric field is directly related to  $1/\Delta Z$ , here we use  $\Delta Z$  of the  $Z$ - $V$  spectra at 9 V to indicate the tunnelling condition, as written at the left-hand side of each spectrum. The electric field is thus strongest while the spectrum corresponding to the smallest  $\Delta Z$  was acquired. Consequently, the energy levels of the Gundlach oscillation peaks in this spectrum, as indicated by dashed lines, are higher than the other two spectra. This observation can be interpreted with the model of quantized states formed in a potential well in the tip-sample gap [12]. However, we also observe that the energy level of

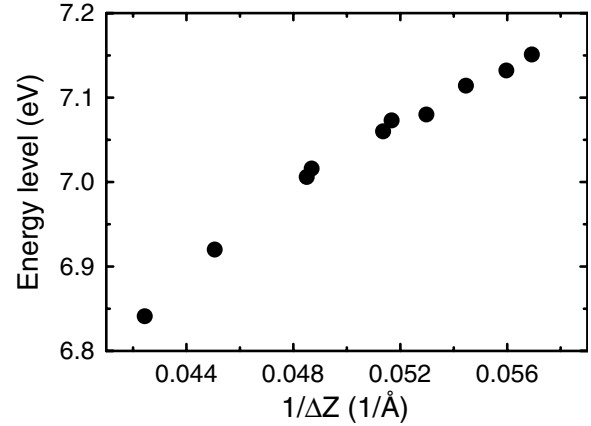


**Figure 21.** Energy levels of the transmission resonance of the 5-layer film as a function of  $1/\Delta Z$ .

the transmission resonance moves towards higher energy with decreasing  $\Delta Z$ , as indicated by the arrows. Figure 21 shows the energy level of the transmission resonance as a function of  $1/\Delta Z$ . Since the electric field is approximately proportional to  $1/\Delta Z$ , Figure 21 implies that the transmission resonance can be monotonically shifted to a high energy with increasing electric field. The shifting is about 290 meV as the set current is adjusted from 0.6 to 10 nA, which is much larger than the shifting of the surface state, i.e. only 1–2 meV, under a similar condition [73].

According to quantum mechanics, the condition for the transmission resonance to occur is

$$2kt = 2n\pi, \quad (10)$$

where  $n$  is an integer,  $k$  is the wavevector of the electron in the square potential well, and  $t$  is the width of the well. In addition,

$$\hbar^2 k^2 / 2m = E + V, \quad (11)$$

where  $E$  is the energy of free electron matching the transmission resonance and  $V$  is the depth of the well. It is interesting to note that equation (10) is exactly the quantization rule of the quantized states in the infinite square well as shown in figure 22(a). For a finite square well as shown in figure 22(b), the quantization rule should include a phase term because the electron in the well can penetrate the potential barrier, and it becomes

$$2kt + 2\phi = 2n\pi. \quad (12)$$

It is known that  $\phi$  can be obtained by the following equation [74]:

$$\phi = 2 \tan^{-1} (\psi' / k\psi), \quad (13)$$

where  $\psi$  and  $\psi'$  are the wavefunction and its derivative on the barrier side.

Since equation (10) is the quantization rule for the transmission resonance of the free electron scattered by a symmetric square well, we analogously introduce an extra phase term in the quantization rule when the electron is in

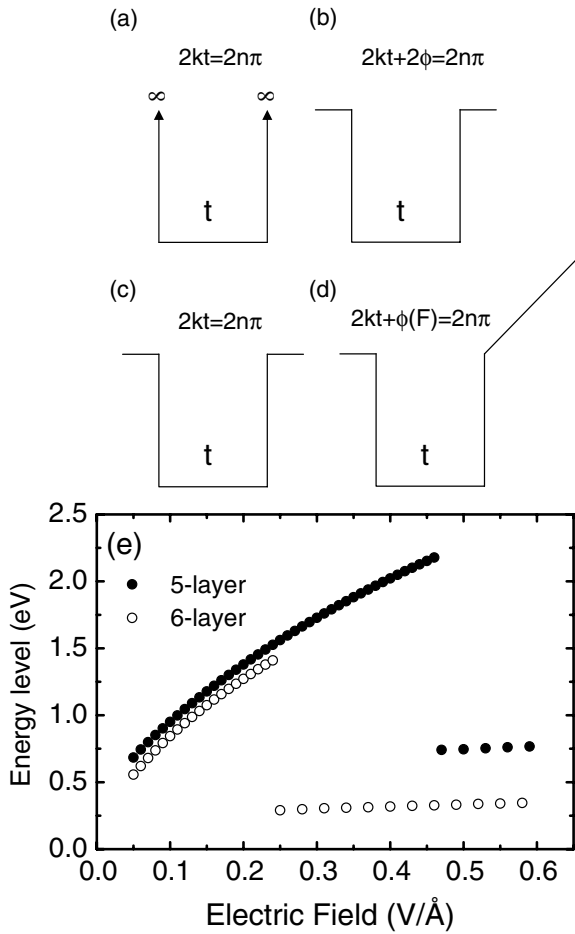


**Figure 22.** Quantization rules for quantized states in (a) infinite square well, (b) finite square well and for transmission resonance in (c) square well, (d) square well combined with an accelerating field. (e) Calculated energy level of the transmission resonance as a function of the electric field for the 5-layer and the 6-layer film.

an accelerating field instead of a free space, as illustrated in figures 22(c) and (d). This phase is field-dependent and we assume that it also obeys equation (13). Since the accelerating field is applied at the vacuum side, the phase only appears at the vacuum/Ag interface and the quantization rule becomes

$$2kt + \phi(F) = 2n\pi. \quad (14)$$

Based on the above arguments, we can calculate the energy level of the transmission resonance at different electric fields. In the calculation, we use the potential form in figure 22(d) to approximate those in the tip-sample gap (triangular potential) and in the Ag film (square potential). It is known that the wavefunction in a triangular potential well [71, 75] is the Airy function  $Ai$  [76]. At the vacuum/Ag interface

$$\psi'/\psi = (2meF/\hbar^2)^{1/3} Ai'(g)/Ai(g), \quad (15)$$

$$g = -(2m)^{1/3} E/(\hbar eF)^{2/3}, \quad (16)$$

where  $E$  is the total energy of electron in the triangular potential and  $F$  is the electric field. Since the transmission resonance is shifted towards higher energies (larger  $k$ ), according to equation (14),  $\phi$  should be negative. In addition,  $V$  is 8 eV [7

and  $t$  is equal to layer-number $\times 2.5 \text{ \AA}$  for a Ag film in the calculation. Using equation (11) and equations (13)–(16) as well as  $n = 6$  and 7 for the 5-layer and 6-layer films, respectively, the variations of the transmission resonance with the electric field for these films are calculated. Figure 22(e) shows that the calculated transmission resonance of the 5-layer film is monotonically shifted to higher energies with the electric field, qualitatively agreeing with our observation. However, the calculation also predicts that beyond a critical field, the transmission resonance should drop to a lower energy discontinuously. This abrupt change comes from the fact that the phase  $\phi$  is limited to the range of 0 to  $-\pi$  for equation (13) and it is negative. Before the appearance of discontinuous drop, the phase is negatively increased with increasing electric field, resulting in the monotonic shifting of the transmission resonance. When the critical electric field is applied, the phase is equal to  $-\pi$ . The phase should return to 0 for preserving a given  $n$  in equation (14) as the electric field exceeds the critical strength, causing a discontinuous drop in the transmission resonance. The calculation also reveals that the shifting after discontinuous drop becomes much slower. This result is due to the fact that with increasing electric field, the changing rate of the Airy function is close to that of its differentiation after the discontinuous drop in the transmission resonance, causing the negative increment of the phase to be slow as the electric field increases. These characteristics of calculated field-dependent transmission resonance are similar for the 6-layer film. However, it is obvious that the critical field of the 6-layer film is much lower than that of the 5-layer film. This implies that the phenomenon of the discontinuous drop, which is not observed on the 5-layer because of the requirement of stronger electric field, may be observable for the 6-layer film.

Figure 23(a) shows the  $dZ/dV-V$  spectra acquired on the 6-layer film at different electric fields. From the withdrawn distance  $\Delta Z$  indicated at the left-hand side of each spectrum, we can know that the electric field of the green curve is stronger than that of the black curve. It is obvious to see that the energy level of the transmission resonance (marked by an arrow) in the green curve is lower than that in the black curve by about 0.4 eV. Furthermore, we did not observe that this lowering of transmission resonance with  $1/\Delta Z$  occurred gradually. The only intermediate situation near the critical electric field, as shown in the red curve, is that the spectral intensity of the transmission resonance is comparable to that of a Gundlach oscillation peak, in which the transmission resonance is hard to be identified. Therefore, the lowering of the transmission resonance is discontinuous as the electric field is beyond a critical field. This is qualitatively consistent with the prediction of the calculation. Figure 23(b) shows the energy level of the transmission resonance of the 6-layer film as a function of  $1/\Delta Z$ , in which a discontinuous drop is observed. When the electric field is below the critical field, the transmission resonance is shifted to higher energies with the electric field, the same as the case on the 5-layer film. After the occurrence of the discontinuous drop, the transmission resonance hardly becomes shifted by the electric field, in agreement with the calculation. In addition, the critical field

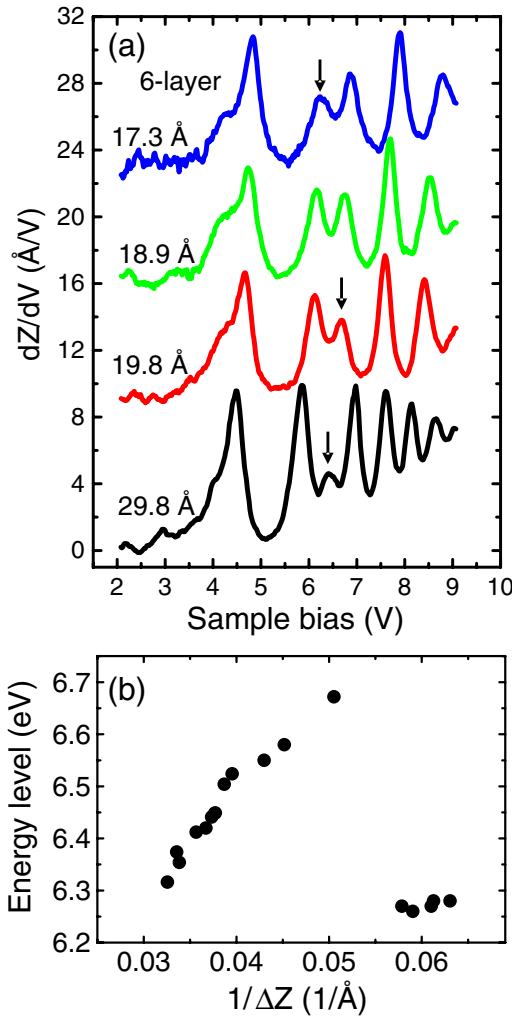


**Figure 23.** (a) The  $dZ/dV-V$  spectra acquired on the 6-layer film at different  $\Delta Z$  (electric field). (b) Energy levels of the transmission resonance of the 5-layer film as a function of  $1/\Delta Z$ . There appears a discontinuous drop in the transmission resonance in energy level.

corresponds to  $1/\Delta Z$  about 0.05 in figure 23(b). This value is in the range of  $1/\Delta Z$  of figure 21 but where there is no observation of the discontinuous drop. This indicates that the critical field of the 6-layer film is indeed weaker than that of the 5-layer film.

The phenomenon of the discontinuous drop in the transmission resonance actually appeared in the work of Kubby *et al* [71]. In figure 6 of their report, the authors shows the spectra acquired on the  $\sqrt{3} \times \sqrt{3}$  Sn/Si(111) surface at the different electric field which can be judged from the number of Gundlach oscillation peaks, i.e. the fewer one indicates a stronger electric field. By carefully identifying the transmission resonance in their spectra, one can find that its energy level at the strongest electric field is lower than that at the weakest electric field. This indicates that the transmission resonance in this system may also experience a discontinuous drop with increasing electric field. In addition, the spectrum acquired at the medium electric field also exhibits the phenomenon of being unable to distinguish the transmission resonance from the nearby Gundlach oscillation peak, similar to our observation.

### 3.3. Peak intensity of the Gundlach oscillation modulated by the interface structure and the surface reconstruction

The Gundlach oscillation [10] observed with  $dZ/dV$  spectroscopy is a phenomenon of field-emission resonance through standing-wave states in the tip-sample gap [11–13]. Although the Gundlach oscillation is a general phenomenon that can be observed on metal surfaces, in comparison with the step-like feature of the Gundlach oscillation in the  $Z-V$  spectrum acquired on Ni(100) [11] it is found that the one acquired on Au(110) is much weaker [12]. This implies that the peak intensity of the Gundlach oscillation depends significantly on the species of the metal, but, to our knowledge, its origin remains to be elucidated. The Gundlach oscillation is not the only phenomenon manifested in the tunnelling spectrum when the surface of thin metal film is observed. As we have shown in section 3.2, the signal of the transmission resonance superposed with the Gundlach oscillation can appear in the tunnelling spectra acquired on the Ag/Si(111)  $7 \times 7$  [24] and the  $\sqrt{3} \times \sqrt{3}$  Sn/Si(111) surfaces [11]. Besides using the scanning spectroscopy, the transmission resonance can also be observed using LEETS [6] for some free-electron-like metal films such as Ag and Cu films [7, 8]. In LEETS and  $dZ/dV$  spectroscopy, electrons with energy matching levels of the transmission resonance can be of higher transmissivity and spectral intensity, respectively. Since both kinds of spectroscopy can be used to observe transmission resonance, it is natural to consider that the information about the transmissivity varied with electron energy in LEETS should be involved in the  $dZ/dV$  spectra. Based on this realization, we propose a model that the spectrum has two components; one is the Gundlach oscillation and the other is a component which provides a significant offset to the Gundlach oscillation. Since the latter is related to the transmissivity, we call it transmission background hereafter<sup>2</sup>. That is, the higher intensity of the transmission background corresponds to the larger transmissivity. In addition, because of the wave nature, the electron impinging on the surface of the metal, no matter if it is the thin film or the bulk, has a probability to transmit. Therefore, the model is applicable to the Gundlach oscillation observed on the bulk surface as well. In this work, we demonstrate that the peak intensity of the Gundlach oscillation may change with the observed location on the Ag/Si(111)  $7 \times 7$  surface and the reconstructed Au(111) surface. According to the proposed model, we can explain that this location-dependent Gundlach oscillation is due to the variation of the transmission background, and is ultimately related to local electron transmissivity. In addition, in these two studied systems, we have found that the total intensity in the range of the Gundlach oscillation is conserved, although its intensity distribution is location dependent. This observation leads to the possibility of understanding why the strength of the Gundlach oscillation depends significantly on the species of the metal. Furthermore, we demonstrate that the transmission background can be correlated with the density of states in

<sup>2</sup> The transmissivity is the probability of electron transmission. The correlation between the transmissivity and the spectral intensity of the transmission background is not clear, and we therefore use ‘equivalent’ to temporarily represent their correlation.

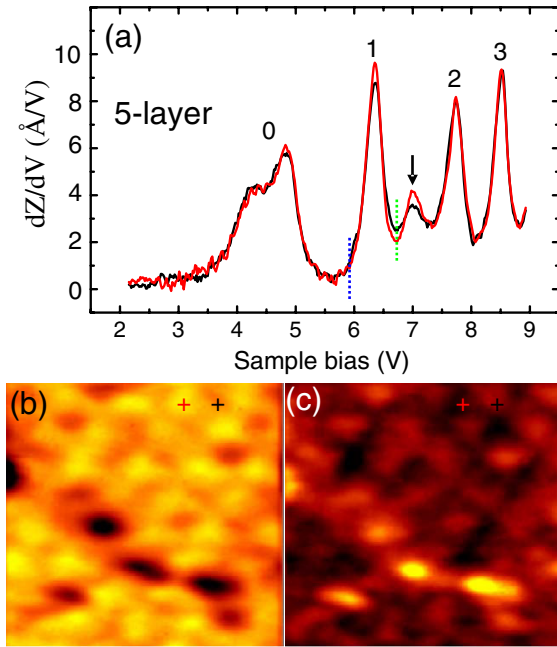


**Figure 24.** (a) Spectra acquired at two locations on the 5-layer film, revealing visible differences. The (blue and green) dotted lines mark the onset and end of peak 1 in the black and red (grey) curves, respectively. The arrow marks the transmission resonance. (b) and (c) show the mappings at the apex (6.35 eV) and the end (6.72 eV) of peak 1, respectively. Crosses mark the locations where the spectra were acquired. The image size is  $120 \times 120 \text{ \AA}^2$ . (Colour online.)

the projected bulk band structure by inspecting the Gundlach oscillation on the Ag(1 0 0) surface.

In this experiment, the Gundlach oscillation was studied for three kinds of metal surfaces. To prepare the Ag film on a Ag/Si(1 1 1) $7 \times 7$  surface, silver was deposited onto the surface at room temperature with a flux of  $0.26 \text{ ML min}^{-1}$ . After deposition, the sample was transferred to a home-built STM operating at 109 K. To prepare clean Au(1 1 1) and Ag(1 0 0) surfaces, samples were treated with cycles of ion beam sputtering and annealing to 600 °C. The Au(1 1 1) and Ag(1 0 0) surfaces were then studied using another home-built STM operating at 4.3 K. The Gundlach oscillation was observed using  $Z$ - $V$  spectroscopy has been described in section 3.2. The  $dZ/dV$ - $V$  spectrum was obtained by numerical differentiation of the  $Z$ - $V$  spectrum. The spatial mapping of intensity of the  $dZ/dV$ - $V$  spectrum at a specific energy was acquired by the numerical method or by combining the lock-in amplifier with a 30 mV bias modulation at 5 kHz.

In section 3.2, we have shown that both the Gundlach oscillation and transmission resonance can be revealed in the tunnelling spectrum taken on the Ag film grown on the Si(1 1 1) $7 \times 7$  surface. Figure 24(a) shows two  $dZ/dV$ - $V$  spectra acquired at two locations on a 5-layer Ag film. The signal indicated by an arrow is the transmission resonance. The distinct peaks marked by numbers are the Gundlach oscillations, and depending on the potential well for forming these peaks, they can be classified. The potential well in the tunnelling gap is a superposition of the image potential and the electrostatic potential [11]. The actual shape of this well varies with the applied voltage while the  $Z$ - $V$  spectroscopy

is being performed. When the Fermi level of the tip is close to the vacuum level of the sample, the contribution of the image potential is significant. The superposition of the image potential and the electrostatic potential forms a specific potential well, and peak 0 is the Gundlach oscillation related to a standing-wave state in this well. When the Fermi level of the tip is higher than the vacuum level of the sample, the image potential becomes negligible, and the potential well can be approximated to be of triangular shape. Referring to the work function of the Ag film on Si(1 1 1) being 4.41 eV [70], peaks 1, 2, 3 are Gundlach oscillations above the vacuum level and can be classified into a group. In this work, we focus only on the Gundlach oscillation above the vacuum level because the correlation between its intensity and the transmissivity of the free electron is concerned. Peak 1 in figure 24(a) is such a Gundlach oscillation, its onset and end are marked by blue and green dashed lines, respectively. The spectra shown in figure 24(a) display visible intensity differences at the transmission resonance, the end and the apex of peak 1. In order to find the origin of the local variation of the spectra, we performed the spatial mapping of the spectral intensity using the lock-in technique. Figures 24(b) and (c) show such mappings at the apex and the end of peak 1. Figure 24(c) has a reversal contrast of figure 24(b) because the spectral intensity of two curves at the end of peak 1 is reversed. Crosses mark the locations where the spectra were acquired, and their colours denote the corresponding spectra in figure 24(a). Interestingly, it can be seen that figure 24(b) exhibits a hexagonal lattice with a period of about  $27 \text{ \AA}$ , in agreement with that of the Si(1 1 1) $7 \times 7$  reconstruction. Therefore, the variations of spectral intensity with locations essentially originate from the Ag/Si(1 1 1) $7 \times 7$  interface property. According to the proposed model, this indicates that the electron transmissivity at the transmission resonance may change with the location due to the modulation of interface property. That is, the local variation of potential barrier affects the electron reflection phase at the buried interface, causing the transmissivity of electrons to vary with the location. This local variation of transmissivity also correspondingly emerges in the transmission background of peak 1. The intensities at the onset of peak 1 in both curves are the same but the intensity at the end of peak 1 in the black curve is larger than that in the red curve. It is plausible to expect that the transmission background in the range of peak 1 in the red curve cannot be higher than that in the black curve. In addition, we measured the total intensity of peak 1 for both curves, and the result indicates that the total intensity of peak 1 is conserved although its intensity distribution is different in each curve. The intensity distribution of the peak is the superposition of the transmission background and the Gundlach oscillation. Since the total intensity of the transmission background of peak 1 in the black curve is larger than that in the red (grey) curve, the total intensity of the Gundlach oscillation of peak 1 in the red curve should be larger due to conservation of the total intensity. This results in the apex of peak 1 in the red curve having a greater intensity. Therefore, the total intensity of the transmission background is complementary to that of the Gundlach oscillation. Next, we will show that this

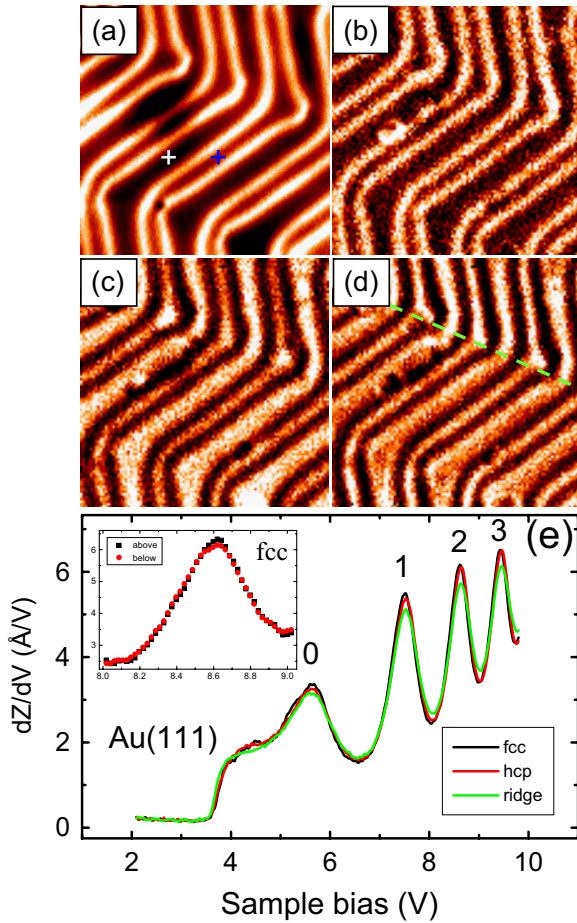


**Figure 25.** (a) Topographical image of a reconstructed Au(111) surface. The image size is  $286 \times 286 \text{ \AA}^2$ . (b) Mapping at the valley (8.06 eV) between peak 1 and peak 2 in (e). (c) and (d) are mappings at the apexes of peak 1 (7.53 eV) and peak 2 (8.64 eV) in (e), respectively. (e) The average  $dZ/dV-V$  spectra of the fcc, hcp and ridge regions. The inset shows peak 2 at fcc regions above and below the dashed line in (d). The pixels of topographical image in (a) are  $500 \times 500$ . The pixels of mappings in (b), (c) and (d) are  $100 \times 100$ . The mappings are smoothed by the interpolation.

complementary phenomenon should be general because it also appears on the Au(111) surface.

Figure 25(a) shows a typical topographical image of the Au(111) surface with the well-known  $22 \times \sqrt{3}$  herringbone reconstruction [77]. In this structure, the bright ridge lines separate the surface into the hcp and the fcc regions, as marked by blue and white crosses in figure 25(a), respectively. Recently, Chen *et al* have demonstrated that the electronic structure of the hcp region differs from that of the fcc region. They observed that there is a striking intensity difference between the two regions in the tunnelling spectra near the surface-state band edge [78]. This observation prompted us to investigate whether the transmission background of two regions is different. We acquire the  $Z-V$  spectra and topographical image simultaneously in order to obtain the spectrum at a precise position. Figure 25(e) shows the average  $dZ/dV-V$  spectra taken at the fcc, hcp and ridge regions. In each spectrum, there are four peaks of the Gundlach oscillation and we will focus on peaks 1, 2, 3. Due to the fact that adjacent peaks overlap, the onset and the end of each peak cannot be

determined as peak 1 in figure 24(a). In our measurements, the energy levels of the valleys between the peaks and the apexes of the peaks for the three regions are the same. However, the intensities at the valleys for the ridge region are all higher than those for the fcc and hcp regions. This implies that the transmission background of the ridge region is always higher than those of the fcc and hcp regions. According to the proposed model, we can infer that the ridge region has the highest electron transmissivity on the reconstructed Au(111) surface. This local variation of transmissivity can reflect on the mapping of the spectral intensity, which is simply the spatial variation of the numerical value of  $dZ/dV$  at a specific bias. Figure 25(b) shows the spectral mapping at the valley between peak 1 and peak 2. It turns out that the bright area (higher intensity) in figure 25(b) corresponds to the ridge region in figure 25(a). Figure 25(e) also reveals the same phenomenon as in figure 24(a): the peak with higher transmission background has a lower intensity at the apex, and vice versa. This indicates that complementary phenomenon also manifests on the Au(111) surface. Figure 25(c), the spectral mapping at the apex of peak 1, thus clearly exhibits a reversal contrast of figure 25(b) as expected. Moreover, figure 25(c) reveals that the contrast at the fcc region is slightly brighter than that at the hcp region, consistent with the spectral intensities of two regions at the apex of peak 1, shown in figure 25(e). Careful identification of the intensities at the valleys around peak 1 indeed verifies that the transmission background in the range of peak 1 at the hcp region is slightly larger than that at the fcc region, again showing the complementary phenomenon. Figure 25(d) shows the spectral mapping at the apex of peak 2. It exhibits that the fcc and hcp regions above the dashed line are brighter than those below it. This can also be verified by the spectra provided in the inset of figure 25(e), where only spectra in the fcc regions are shown. This implies that transmissivity also changes with the orientation of the herringbone reconstruction, which may result from the inhomogeneous relief of the local strain field on the Au(111) surface. We have also observed the complementary phenomenon on the  $9 \times 9 \text{ Ag/Cu}(111)$  [81] and  $11 \times 11 \text{ Pb/Si}(111)$  [23] superstructures, and therefore believe that the complementary phenomenon is a general one when the surface is covered uniformly with the same material. Hence, it can be known now that once the electron transmissivity is periodically varied with the interface structure and the surface reconstruction, the peak intensity of the Gundlach oscillation will be modulated.

Figure 26 demonstrates the  $dZ/dV-V$  spectrum acquired on a  $\text{Ag}(100)$  surface, in which six peaks of Gundlach oscillation were observed, as marked by numbers. Peak 1 is the one we are interested in because the spectral intensities are zero at its onset and end, marked by blue and green dashed lines, respectively. This indicates that the intensity of the transmission background is also zero in the distribution of peak 1, and therefore peak 1 is a pure Gundlach oscillation without transmission background. Brown and grey dashed lines mark the end of peak 0 and the onset of peak 2. It can clearly be seen that the spectral intensity is zero in the range between the brown and the blue dashed lines, as well as in the

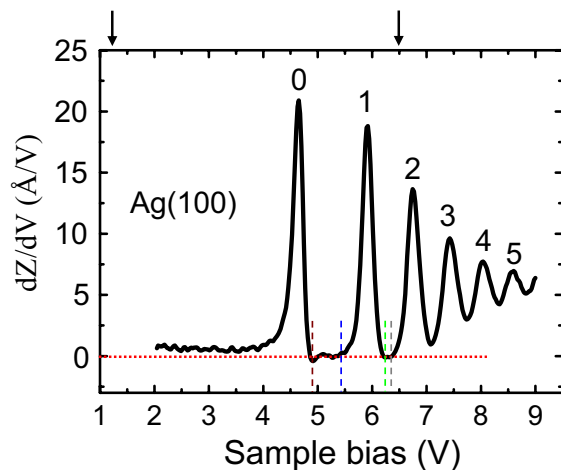


**Figure 26.** The  $dZ/dV-V$  spectrum acquired on an Ag(100) surface. Downward arrows mark the range of the band gap. Red, brown, blue, green and grey dashed lines mark the level of zero intensity, the end of peak 0, the onset of peak 1, the end of peak 1 and the onset of peak 2, respectively. (Colour online.)

one between the green and the grey dashed lines. According to the proposed model, we can therefore conclude that the electron transmissivity is zero in the energy range between the brown and the grey dashed lines. This region without transmission background is in the band gap of the projected bulk band structure of the Ag(100) face [80]. Two downward arrows in figure 26 mark the range of the band gap. Previous studies have demonstrated that the transmissivity of the free electron impinging on some crystal surfaces is reduced when the electron energy coincides with the energy level of the band gap in the band structure [81]. This implies that the density of states would be the channel for electron transmission because it is zero in the band gap, causing the decrease in transmissivity. Therefore, the transmission background with zero intensity in the spectrum essentially originates from the band gap. In other words, it is plausible to consider that the transmission background can directly reflect the electronic density of states at the surface. Based on this opinion, the transmission resonance may originate from the existence of an oscillatory distribution of the density of states in the electronic structure of the metal film. The transmission resonance corresponds to the energy level at which the density of states is at a maximum. Since the transmission background can be correlated with the density of states of the surface, it is why the strength of the Gundlach oscillation depends significantly on the species of the metal. Although the density of states can be probed using STS, which can be well described by the models of metal–vacuum metal tunnelling [82, 83] only when the applied bias is in the range between  $-2$  and  $2$  V. In our experiment, we have applied the sample bias above the vacuum level of the sample to probe the transmission background. The energy range is beyond the range that those models are applied to. In addition, Becker *et al* [12] has mentioned that if the applied bias exceeds the work function of the sample, field emission will appear on the tip. Therefore, the manifestation of the transmission background in the tunnelling spectrum cannot be described by the model of metal–vacuum–metal tunnelling. A more

sophisticated model including the factors of field emission is needed.

#### 4. Application of the Gundlach oscillation on work function measurement of thin metallic films

The work function measurement of a metal film with a broad beam technique, such as photoemission, demands the metal film being grown in a layer-by-layer mode; otherwise what has been measured is just an average result over the films of various thicknesses. In order to overcome this limitation, a local probe technique such as STM is an option without the need for a uniform film. Using STM, one can obtain the work function of the metal surface by measuring the apparent barrier height [84]. Nevertheless, the general measured error with this method can be as high as  $0.3$  eV, much inferior to the precision achievable by the broad beam technique. An alternative choice is to observe the Gundlach oscillation [10] in  $dZ/dV$  spectroscopy. Schintke *et al* are the first to propose the energy shift (ES) between the lowest-order peaks of Gundlach oscillations on the MgO film and the Ag(100) substrate as the difference in their work functions [85]. Recently, Pivetta *et al* also measured the ES of the lowest order on the moiré pattern of NaCl films on Ag(100) and interpreted it as the variation of the local work function of the NaCl film [86]. However, both measurements do not agree with the density function calculations [86, 87]. Therefore, it cannot be certain whether the Gundlach oscillation can really be a way to measure the work function of thin films. In this work, we study the Gundlach oscillation of Ag/Au(111), Ag/Cu(111) and Co/Cu(111) systems. Our results extract a general phenomenon that the peaks of the Gundlach oscillation taken on the film and the substrate are separated by a constant value, except the one of the lowest order. This constant ES, in principle, is the work function difference of the thin metal film and the substrate. With this new establishment, inconsistency between the theoretical calculations and experimental results of the previous studies can be clarified as well.

In our experiment, we use a home-built STM operating at  $4.3$  K to acquire the  $Z-V$  spectrum to observe the Gundlach oscillation. Differentiation of the  $Z-V$  spectrum was performed by a numerical method. The inset in figure 27(a) shows a typical STM topography image of a submonolayer Ag film grown on the Au(111) surface with the well-known  $22 \times \sqrt{3}$  herringbone reconstruction [77]. Areas without reconstruction lines are the Ag film. The curves in figure 27(a) are the average  $dZ/dV-V$  spectra taken on the Ag and Au regions, respectively. Both spectra display clear Gundlach oscillations. The numbers marked close to the peaks denote the order of a Gundlach oscillation. The energy levels of the peaks on the Au surface are all higher than the ones on the Ag film for the same order. Figure 27(c) shows that the ES between the same order peak as a function of the order, marked by open squares. To measure the ES, the peaks of the substrate are used as the reference. It can be seen that the ES of the first order, about  $-0.47$  eV, is the same as that of the second order but that of the lowest (zero) order is obviously different. The inset in figure 27(b) exhibits the STM image of

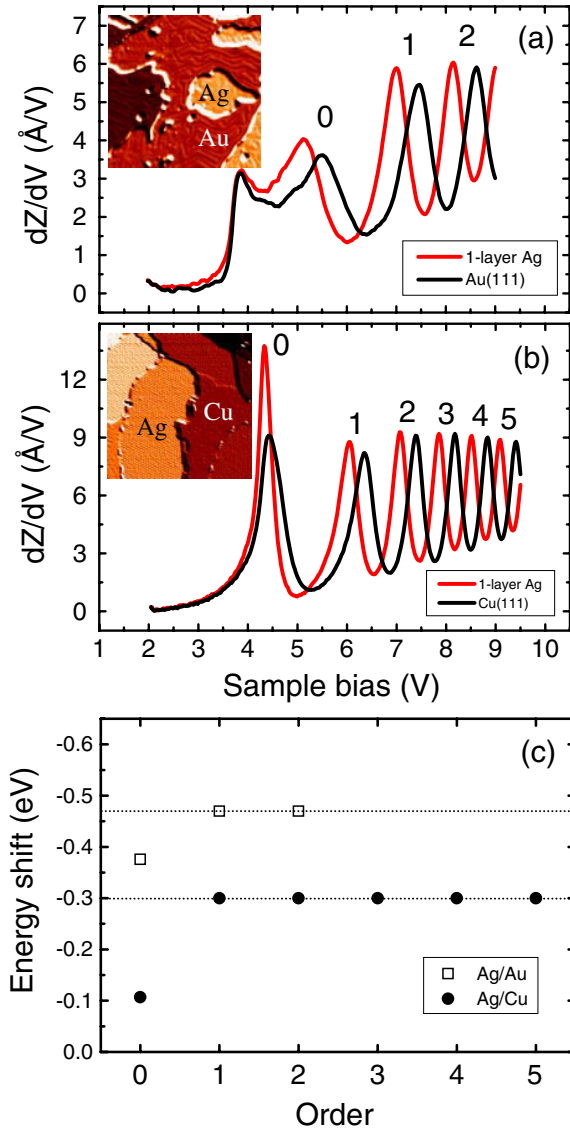


**Figure 27.** (a) The average  $dZ/dV-V$  spectra of the Ag and Au regions. Distinct peaks marked by numbers are Gundlach oscillations. Inset: STM image of submonolayer Ag film grown on the Au(1 1 1) surface. (b) The average  $dZ/dV-V$  spectra of the Ag and Au regions. Inset: STM image of the submonolayer Ag film grown on the Cu(1 1 1) surface. (c) Energy shift between peaks of the same order as a function of the order for spectra in (a) and (b). The peaks of the substrate are used as the reference. Dashed lines mark the constant energy shifts.

a submonolayer Ag film grown on the Cu(1 1 1) surface. Areas with a  $9 \times 9$  superstructure [79] are the Ag film. The curves in figure 27(b) show the average  $dZ/dV-V$  spectra of the Ag and Cu regions, and again the energy levels of the peaks on the Cu region are always higher than the ones on the Ag regions for the same order. The ES as a function of the order, indicated by solid circles in figure 27(c), shows the same situation that the ES of all orders is a constant value of  $-0.3$  eV, except that of the lowest order. We also observe the constant ES on the Co/Cu(1 1 1) system [88], and therefore believe that the constant ES is a general phenomenon. As we have mentioned in section 3.3, the lowest-order peak is the standing wave state in a potential well which is the superposition of image potential

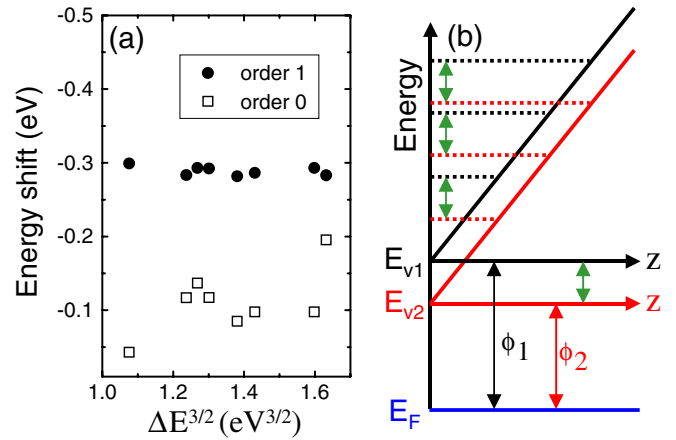


**Figure 28.** (a) Energy shifts of the orders 0 and 1 as a function of  $\Delta E^{3/2}$  for the Ag/Cu(1 1 1) system, and  $\Delta E$  is the energy difference between the orders 1 and 2. (b) Schematic illustration of the energy level  $E_n$  of the standing-wave state (dashed line) in the triangular potential well for different work functions  $\phi_1$  and  $\phi_2$ . With respect to the Fermi level,  $E_n = \phi + (\hbar^2/2m)^{1/3} (3\pi eF/2)^{2/3} (n - 1/4)^{2/3}$ ,  $n = 1, 2, 3, \dots$ , where  $\phi$  is the work function and  $F$  is the electric field. When the electric field is the same, the work function difference ( $\phi_1 - \phi_2$ ) is equal to the energy shift of the same order standing-wave state.

and applied potential, and those peaks of higher order are related to the standing-wave states in the potential well close to the triangular shape. Derivation based on quantum mechanics shows that the energy difference of the standing wave states in the triangular well is proportional to  $F^{2/3}$  [71], where  $F$  is the electric field in the tip-sample gap. In STM, one can adjust the tunnelling current to tune the electric field [25, 73]. Therefore, an interesting issue is whether the constant ES is varied with the electric field. Figure 28(a) shows the ES of the orders 0 and 1 as a function of  $\Delta E^{3/2}$ , which is proportional to the electric field, for the Ag/Cu(1 1 1) system, and  $\Delta E$  is the energy difference between orders 1 and 2. It can be seen that the ES of order 1 is nearly independent of the electric field but the ES of order 0 reveals a large variation with the electric field. The position of the lowest-order peak relative to the vacuum level is basically determined by the shape of the well and the crystal phase at the metal-vacuum interface [89]. Since the image potential is supposed to be the same for the metal film and the substrate, the well shape will change with the electric field, i.e. the tip-sample distance. Because the densities of states of the film and the substrate are different in general, it can be expected that the tip retracting trajectories will follow different routes while the bias voltage is ramping. In addition, the crystal phase also varies with the material [90]. Based on these realizations, the ES of the lowest-order peak is sensitive to the electric field as shown in figure 28(a), and it cannot reflect the work function alone. In contrast, manifestation of the constant ES for peaks of higher order implies that the electric field on the film is the same as that on the substrate. Therefore, the constant ES signifies the separation of the vacuum levels of the film and the substrate, i.e. the work function difference, as schematically illustrated in figure 28(b). For this reason, the work function of a metal film can be measured with the constant ES as long as that of

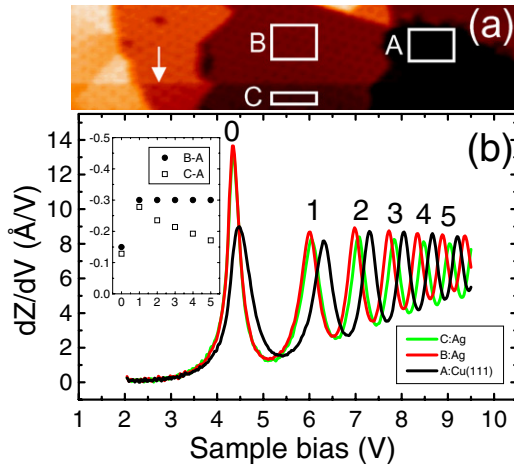


**Figure 29.** (a) STM image of the submonolayer Ag film grown on Cu(111) surface. The arrow marks the contrast discontinuity in the image. (b) The average  $dZ/dV-V$  spectra of areas A, B, C are indicated in (a). Inset: energy shift as a function of the order for spectra at A and B areas (solid circle) and at A and C areas (open square).

the metal substrate is given. Moreover, the change in the work function for the adsorption of one monolayer Ag film on the Cu(111) surface was 0.33 eV measured with photoemission spectroscopy [91]. This is quite close to the 0.3 eV measured here using the Gundlach oscillation, showing the consistency of these two techniques. The constant ES actually appeared in the work of Pivetta *et al* [86]. In figure 2(f) of their paper, the authors show the spectra acquired on the bright and dark regions of the NaCl film on Ag(100). By carefully measuring the ES of higher order peaks, we find that they are almost the same, and are about twice the ES of the lowest-order peak. This indicates that the phenomenon of constant ES can also appear on an insulator film grown on a metal substrate. Owing to that, the authors used the lowest-order ES as the difference of the local work function, and they concluded that their measurement was inconsistent with the theoretical calculation [86] in which the derived value is also about twice the lowest-order ES. According to our current understanding, however, the theoretical calculation should have been quite close to the experimental result if the ES of higher order was used.

Figure 29(a) is the image of Ag films grown on the Cu(111) surface, and, as one can see, there exists a contrast discontinuity as marked by an arrow, originating from the abrupt structure change at the tip apex. Figure 29(b) shows the average  $dZ/dV-V$  spectra acquired on areas A, B, C indicated in figure 29(a). Although areas B and C are on the Ag film, the peak positions in the corresponding spectra in figure 29(b) are not identical. This is due to the abrupt change in the tip condition that significantly affects the electric field to be different at areas B and C. Area A is on the Cu surface; the tip condition for acquiring spectra at this area is the same as that at area B but is different from that at area C. Therefore, except for the zero order, the ES (solid circle) is a constant of -0.3 eV for all orders for spectra at A and B areas, but the ES (open square) is decreased with the order for spectra at A and C areas, as shown in the inset in figure 29(b). These

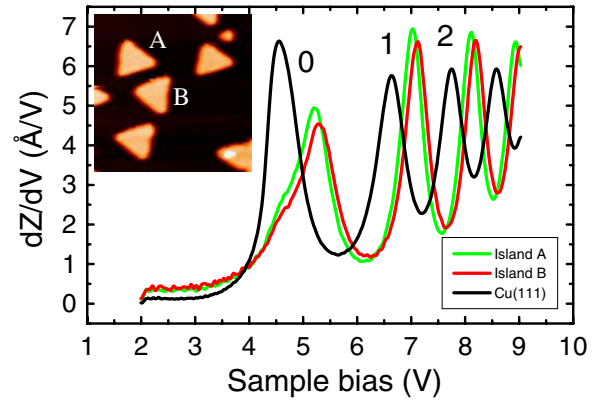


**Figure 30.** The average  $dZ/dV-V$  spectra acquired on the Cu surface, Co islands A and B marked in the inset: STM image of Co islands grown on the Cu(111) surface.

observations reveal that the work function measurement with the Gundlach oscillation basically requires a high stability of the tip condition. Although the change in the tip condition may affect the work function measurement, the inset in figure 29(b) reveals that one can still use the ES of the order next to the lowest order to estimate the work function because it is the closest one to the constant ES. This enables us to estimate the work function reduction in the MgO film grown on Ag(100) from the work of Schintke *et al* [85]. In figure 2(c) of their paper, the authors show the spectra acquired on the 1-layer MgO film and the Ag(100) substrate. Since the electric fields on the MgO film and on the Ag surface are different, there is no constant ES in spectra. According to our current realization, the ES of peak 2 would be close to the real work function reduction, which is about 1.1 eV. This value is actually in agreement with the value of 1.01 eV calculated by the density function calculation [87].

Since Gundlach oscillations manifest as a series of sharp peaks, one can identify the peak position without ambiguity, and hence the work function of the metal film can be measured with high precision. In our observation, the precision of the measurement can be better than 0.02 eV, which is much better than that of detecting apparent barrier height with STM and is comparable to the photoemission results. This allows us to detect the subtle variation of the work function for some nanostructures. For instance, it is well known that Co islands with a triangular shape can be formed on the Cu(111) surface at room temperature [88] as shown in the inset in figure 30. The curves in figure 30 show the average  $dZ/dV-V$  spectra acquired on the Cu surface, and Co islands A and B in the inset. It is obvious that there is a slight shift between the spectra of islands A and B in spite of the same size of the two islands, indicating the work function of island B is higher than that of island A by 0.1 eV. This minute variation of the work function may be attributed to the different stacking sequences between the islands of A and B [88].

## 5. Summary

This review summarizes some recent STM and scanning spectroscopic studies of the QSE in Pb and Ag films. For

Pb films, we have shown that its growth behaviour at low temperature is quite different from the conventional one, and reveals the characteristics of preferred thickness, 2D growth, and 3D-to-2D growth transition. These features originate from the manifestation of the quantum-well state. Although the QSE significantly affects the growth of the Pb film, we have also shown that its nucleation process is similar to that in the homoepitaxy system. Therefore, the area distribution of Pb islands can be analysed by scaling theory and the critical size can be obtained. Moreover, we have demonstrated that the quantum-well states in Pb islands can be detected by the scanning spectroscopic technique. Their strength is spatially modulated when the film is of periodic distortion. For Ag films, we have shown that the phenomenon of the QSE above the vacuum level, i.e. the transmission resonance, can be revealed with  $dZ/dV$  spectroscopy. The energy level of the transmission resonance is thickness dependent and can be shifted by the electric field. The behaviour of the Stark shift can qualitatively explained by introducing a field-dependent phase in the quantization rule. We have also studied the QSE in the tunnelling gap of STM, i.e. the phenomenon of the Gundlach oscillation. We have found that the peak intensity of the Gundlach oscillation can be modulated by the interface structure and surface reconstruction, which contributed to the local variation of the electron transmissivity. Finally, we have found that higher order peaks of the Gundlach oscillation observed on the metal film and the substrate manifest a phenomenon of constant energy shift, which can be used to accurately measure the work function of an ultra-thin metallic film.

## Acknowledgments

The authors would like to appreciate the valuable contributions of S H Chang, W B Jian, H Y Lin, Y P Chiu, S M Lu, H T Shih, C L Jiang, M C Yang and C L Lin. This work was supported by the National Science Council, Academia Sinica, and the project of Academic Excellence of the Ministry of Education of Taiwan.

## References

- [1] Evans D A, Alonso M, Cimino R and Horn K 1993 *Phys. Lett. Rev.* **70** 3483
- [2] Paggel J J, Miller T and Chiang T-C 1999 *Science* **283** 1709
- [3] Kawakami R K, Rotenberg E, Choi H J, Escorcia-Aparicio E J, Bowen M O, Wolfe J H, Arenholz E, Zhang Z D, Smith N V and Qiu Z Q 1999 *Nature* **398** 132
- [4] Mans A, Dil J H, Ettema A R H F and Weitering H H 2002 *Phys. Rev. B* **66** 195410
- [5] Zhang Y F, Jia J F, Han T Z, Tang Z, Shen Q T, Guo Y, Qiu Z Q and Xue Q K 2005 *Phys. Rev. Lett.* **95** 096802
- [6] Sanche M, Bader G and Caron L G 1982 *J. Chem. Phys.* **76** 4016
- [7] Jonker B T, Bartelt N C and Park R L 1983 *Surf. Sci.* **127** 183
- [8] Chung W F, Feng Y J, Poon H C, Chan C T, Tong S Y and Altman M S 2003 *Phys. Rev. Lett.* **90** 216105
- [9] Binnig G and Rohrer H 1987 *Rev. Mod. Phys.* **59** 615
- [10] Gundlach K H 1966 *Solid State Electron.* **9** 949
- [11] Kubby J A, Wang Y R and Greene W J 1990 *Phys. Rev. Lett.* **65** 2165
- [12] Binnig G, Frank K H, Fuchs H, Garcia N, Reihl B, Rohrer H, Salvan F and Williams A R 1985 *Phys. Rev. Lett.* **55** 991
- [13] Becker R S, Golovchenko J A and Swartzentruber B S 1985 *Phys. Rev. Lett.* **55** 987
- [14] Wahl P, Schneider M A, Diekhoner L, Vogelgesang R and Kern K 2003 *Phys. Rev. Lett.* **91** 106802
- [15] Smith A R, Chao K J, Niu Q and Shih C K 1996 *Science* **273** 226
- [16] Gavioli L, Kimberlin K R, Tringides M C, Wendelken J F and Zhang Z 1998 *Phys. Rev. Lett.* **82** 129
- [17] Budde K, Abram E, Yeh V and Tringides M C 2000 *Phys. Rev. B* **61** R10602
- [18] Sobotík P, Ošťádal I, Mysliveček J, Jarolímeček T and Lavický F 2001 *Surf. Sci.* **482–485** 797
- [19] Su W B, Chang S H, Jian W B, Chang C S, Chen L J and Tsong T T 2001 *Phys. Rev. Lett.* **86** 5116
- [20] Chang S H, Su W B, Jian W B, Chang C S, Chen L J and Tsong T T 2002 *Phys. Rev. B* **65** 245401
- [21] Su W B, Chang S H, Lin H Y, Chiu Y P, Fu T Y, Chang C S and Tsong T T 2003 *Phys. Rev. B* **68** 033405
- [22] Su W B, Lin H Y, Chiu Y P, Shih H T, Fu T Y, Chen Y W, Chang C S and Tsong T T 2005 *Phys. Rev. B* **71** 073304
- [23] Lu S M, Yang M C, Su W B, Jiang C L, Hsu T, Chang C S and Tsong T T 2007 *Phys. Rev. B* **75** 113402
- [24] Su W B, Lu S M, Shih H T, Jiang C L, Chang C S and Tsong T T 2006 *J. Phys.: Condens. Matter* **18** 6299
- [25] Su W B, Lu S M, Jiang C L, Shih H T, Chang C S and Tsong T T 2006 *Phys. Rev. B* **74** 155330
- [26] Su W B, Lu S M, Lin C L, Shih H T, Jiang C L, Chang C S and Tsong T T 2007 *Phys. Rev. B* **75** 195406
- [27] Lin C L, Lu S M, Su W B, Shih H T, Wu B F, Yao Y D, Chang C S and Tsong T T 2007 *Phys. Rev. Lett.* **99** 216103
- [28] Lay G L, Peretti J, Hanbücken M and Yang W S 1988 *Surf. Sci.* **204** 57
- [29] Ganz E, Xiong F, Hwang I-S and Golovchenko J 1991 *Phys. Rev. B* **43** 7316
- [30] GomezRodriguez J M, Veuillen J Y and Cinti R C 1996 *J. Vac. Sci. Technol. B* **14** 1005
- [31] Weitering H H, Heslinga D R and Hibma T 1992 *Phys. Rev. B* **45** 5991
- [32] Seehofer L, Falkenberg G, Daboul D and Johnson R L 1995 *Phys. Rev. B* **51** 13503
- [33] Horikoshi K, Tong X, Nagao T and Hasegawa S 1999 *Phys. Rev. B* **60** 13287
- [34] Ganz E, Hwang I S, Xiong F, Theiss S K and Golovchenko J A 1991 *Surf. Sci.* **257** 259
- [35] Hwang I-S, Martinez R E, Liu C and Golovchenko J A 1995 *Surf. Sci.* **323** 241
- [36] Heslinga D R, Weitering H H, van der Werf D P, Klapwijk T M and Hibma T 1990 *Phys. Rev. Lett.* **64** 1589
- [37] Zhang Z, Niu Q and Shih C K 1998 *Phys. Rev. Lett.* **80** 5381
- [38] Schulte F K 1976 *Surf. Sci.* **55** 427
- [39] Jaklevic R C, Lambe J, Mikkor M and Vassell W C 1971 *Phys. Rev. Lett.* **26** 88
- [40] Marliere C 1990 *Vacuum* **41** 1192
- [41] Jalochofski M and Bauer E 1988 *Phys. Rev. B* **38** 5272
- [42] Jalochofski M, Knoppe H, Lilienkamp G and Bauer E 1992 *Phys. Rev. B* **46** 4693
- [43] Miller T, Samsavar A, Franklin G E and Chiang T C 1988 *Phys. Rev. Lett.* **61** 1404
- [44] Hinch B J, Koziol C, Toennies J P and Zhand G 1989 *Europhys. Lett.* **10** 341
- [45] Crottini A, Cvetko D, Floreano L, Gotter R, Morgante A and Tommasini F 1997 *Phys. Rev. Lett.* **79** 1527
- [46] Luh D A, Miller T, Paggel J J, Chou M Y and Chiang T C 2001 *Science* **292** 1131
- [47] Guo Y *et al* 2004 *Science* **306** 1915
- [48] Eom D, Qin S, Chou M Y and Shih C K 2006 *Phys. Rev. Lett.* **96** 027005

- [49] Chan T L, Wang C Z, Hupalo M, Tringides M C and Ho K M 2006 *Phys. Rev. Lett.* **96** 226102
- [50] Ma L Y *et al* 2006 *Phys. Rev. Lett.* **97** 266102
- [51] Jeffrey C A, Conrad E H, Feng R, Hupalo M, Kim C, Ryan P J, Miceli P F and Tringides M C 2006 *Phys. Rev. Lett.* **96** 106105
- [52] Fu Y S *et al* *Phys. Rev. Lett.* **99** 256601
- [53] Lin H Y, Chiu Y P, Huang L W, Chen Y W, Fu T Y, Chang C S and Tsong T T 2005 *Phys. Rev. Lett.* **94** 136101
- [54] Zhang Y F, Tang Z, Han T Z, Ma X, Jia J F, Xue Q K, Xun K and Wu S C 2007 *Appl. Phys. Lett.* **90** 093120
- [55] Jalochowski M and Bauer E 1988 *J. Appl. Phys.* **63** 4501
- [56] Venables J A 1973 *Phil. Mag.* **27** 697
- [57] Strosio J A, Pierce D T and Dragoset R A 1993 *Phys. Rev. Lett.* **70** 3615
- [58] Strosio J A and Pierce D T 1994 *Phys. Rev. B* **49** 8522
- [59] Tsui F, Wellman J, Uher C and Clarke R 1996 *Phys. Rev. Lett.* **76** 3164
- [60] Amar J G and Family F 1995 *Phys. Rev. Lett.* **74** 2066
- [61] Yeh V, Berbil-Bautista L, Wang C Z, Ho K M and Tringides M C 2000 *Phys. Rev. Lett.* **85** 5158
- [62] Altfeder I B, Matveev K A and Chen D M 1997 *Phys. Rev. Lett.* **78** 2815
- [63] Horn K, Reihl B, Zartner A, Eastman D E, Hermann K and Noffke J 1984 *Phys. Rev. B* **30** 1711
- [64] Jian W B, Su W B, Chang C S and Tsong T T 2003 *Phys. Rev. Lett.* **90** 196603
- [65] Hupalo M, Yeh V, Chan T L, Wang C Z, Ho K M and Tringides M C 2005 *Phys. Rev. B* **71** 193408
- [66] Chan T L, Wang C Z, Hupalo M, Tringides M C, Lu W C and Ho K M 2006 *Surf. Sci.* **600** L179
- [67] Kittel C 1986 *Introduction to Solid State Physics* (New York: Wiley)
- [68] Altfeder I B, Narayanamurti V and Chen D M 2002 *Phys. Rev. Lett.* **88** 206801
- [69] Liboff R L 1980 *Introductory Quantum Mechanics* (Reading, MA: Addison-Wesley) p 224
- [70] Thanailakis A 1975 *J. Phys. C: Solid State Phys.* **8** 655
- [71] Kubby J A and Greene W J 1993 *Phys. Rev. B* **48** 11249
- [72] Lu S M, Shih H T, Jiang C L, Su W B, Chang C S and Tsong T T 2006 *Chin. J. Phys. (Taipei)* **44** 309
- [73] Limot L, Maroutian T, Johansson P and Berndt R 2003 *Phys. Rev. Lett.* **91** 196801
- [74] Smith N V and Woodruff D P 1986 *Prog. Surf. Sci.* **21** 295
- [75] Ando T, Fowler A B and Stern F 1982 *Rev. Mod. Phys.* **54** 437
- [76] See, for example Abramowitz M and Stegun I A (ed) 1964 *Handbook of Mathematical Functions* (Washington, DC: US GPO) chapter 10
- [77] Barth J V, Brune H, Ertl G and Behm R J 1990 *Phys. Rev. B* **42** 9307
- [78] Chen W, Madhavan V, Jamneala T and Crommie MF 1998 *Phys. Rev. Lett.* **80** 1469
- [79] McMahon W E, Hirschorn E S and Chiang T-C 1992 *Surf. Sci.* **279** L231
- [80] Schuppler S, Fischer N, Fauster Th and Steinmann W 1992 *Phys. Rev. B* **46** 13539
- [81] Jaklevic R C and Davis L C 1982 *Phys. Rev. B* **26** 5391
- [82] Tersoff J and Hamann D R 1985 *Phys. Rev. B* **31** 805
- [83] Lang N D 1986 *Phys. Rev. B* **34** 5947
- [84] Jia J F, Inoue K, Hasegawa Y, Yang W S and Sakurai T 1998 *Phys. Rev. B* **58** 1193
- [85] Schintke S, Messerli S, Pivetta M, Patthey F, Libiouille L, Stengel M, Vita A S and Schneider W-D 2001 *Phys. Rev. Lett.* **87** 276801
- [86] Pivetta M, Patthey F, Stengel M, Baldereschi A and Schneider W D 2005 *Phys. Rev. B* **72** 115404
- [87] Giordano L, Cinquini F and Pacchioni G 2006 *Phys. Rev. B* **73** 045414
- [88] Vázquez de Parga A L, García-Vidal F J and Miranda R 2000 *Phys. Rev. Lett.* **85** 4365
- [89] Smith N V 1985 *Phys. Rev. B* **32** 3549
- [90] Chulkov E V, Silkin V M and Echenique P M 1999 *Surf. Sci.* **437** 330
- [91] Wallauer W and Fauster Th 1995 *Surf. Sci.* **331** 731